

# Radiation belt model including semi-annual variation and Solar driving (Sentinel)

C. Katsavrias<sup>1,2</sup>, S. Aminimalragia-Giamini<sup>1,2</sup>, C. Papadimitriou<sup>1,2</sup>, I. A.  
Daglis<sup>1,3</sup>, I. Sandberg<sup>2</sup>, and P. Jiggins<sup>4</sup>,

<sup>1</sup>Department of Physics, National and Kapodistrian University of Athens, Greece

<sup>2</sup>Space Applications and Research Consultancy (SPARC), Athens, Greece

<sup>3</sup>Hellenic Space Center, Athens, Greece

<sup>4</sup>ESA/ESTEC, Netherlands

## Key Points:

- A machine learning model is developed to predict the electron fluxes in the outer belt in a broad energy (0.033-4.062 MeV) at 2.5L-5.9.
- The model requires as input solar wind parameters and the Russell-McPherron's angle, which are available in near-real time.
- The model's accuracy is high even outside the L-shell training scheme (GEO) and outside the time interval used for the training.

---

Corresponding author: Christos Katsavrias, [ckatsavrias@phys.uoa.gr](mailto:ckatsavrias@phys.uoa.gr)

## Abstract

The Earth's outer radiation belt response to geospace disturbances is extremely variable spanning from a few hours to several months. In addition, the numerous physical mechanisms, which control this response, depend on the electron energy, the time-scale and the various types of geospace disturbances. As a consequence, the various models that currently exist are either specialized, orbit-specific data-driven models, or sophisticated physics-based ones. In this paper we present a new approach for radiation belt modelling using Machine Learning methods driven solely by solar wind speed and pressure, Solar flux at 10.7 cm and the  $\theta$  angle controlling the Russell-McPherron effect. We show that the model can successfully reproduce and predict the electron fluxes of the outer radiation belt in a broad energy (0.033–4.062 MeV) and L-shell (2.5–5.9) range and, moreover, it can capture the long-term modulation of the semi-annual variation. We also show that the model can generalize well and provide successful predictions, even outside of the spatio-temporal range it has been trained with, using  $\sim$ 0.8 MeV electron flux measurements from GOES-15/EPEAD at geostationary orbit.

## Plain Language Summary

The electron populations of the outer radiation belt are known to present hazards to spacecraft, from instrumentation errors and physical damage to complete loss. The physical mechanisms which control the variability of the population depend on various physical parameters and, as a consequence, the various prediction models that currently exist are either specialized, orbit-specific data-driven models, or sophisticated physics-based ones. In this paper we present a new approach for radiation belt modelling using Machine Learning methods, driven solely by solar wind speed and pressure, Solar flux at 10.7 cm and the  $\theta$  angle controlling the Russell-McPherron effect. We show that the model cannot only successfully reproduce and predict the electron fluxes of the outer radiation belt in a broad energy and spatio-temporal range but also, that it can generalize well and provide successful predictions, even outside of the spatio-temporal range it has been trained with. Its applicability also extends to the provision of reliable predictions of the boundary conditions in physics-based models.

## 1 Introduction

The dynamics of the outer radiation belt are driven by a complex interplay between acceleration and loss mechanisms (Reeves & Daglis, 2016; Daglis et al., 2019) leading to a broad energy range of energetic electrons. These electron populations in the outer belt are known to present hazards to spacecraft. Source ( $\approx$  10–100 keV) and seed ( $\approx$  100–300 keV) electrons can accumulate at the surface of a spacecraft leading to adverse effects such as instrumentation errors and physical damage due to the surface charging effects (Thomsen et al., 2013; Zheng et al., 2019). Furthermore, seed electrons act as a 'reservoir' which can be further accelerated to relativistic energies (Jaynes et al., 2015; W. Li et al., 2016; Katsavrias, Daglis, & Li, 2019; Katsavrias, Sandberg, et al., 2019; Nasi et al., 2020) via the interaction with whistler chorus waves that the source population produces. These relativistic (typically  $>0.5$  MeV) electrons can penetrate through satellite shielding potentially causing internal charging, also leading to satellite loss in extreme cases. Even though the aforementioned populations vary primarily in scales of several hours or days, the relativistic electron fluxes in the outer radiation belt also exhibit variations on longer time scales exhibiting an annual as well as a semi-annual periodicity—henceforward SAV (Baker et al., 1999)—which has been recently shown to be driven by the Russell-McPherron effect (Katsavrias, Papadimitriou, et al., 2021).

Several efforts have been focused on modelling the aforementioned variations and these efforts typically fall into one of two categories, either empirical, data-driven models or physics-based ones. Empirical modelling begun at the dawn of the space age at

the early 60's, using the very first particle radiation satellite data under NASA's Trapped Radiation Environment Model Program (TREMPE) producing the long series of successful models AE1 up to AE8 in 1991 (Vette, 1991), the latter of which are still considered the industry standards. The latest incarnation in this long series of US models is the AE9 model (Ginet et al., 2013), which were first produced in 2012 by the US Air Force Research Laboratory (AFRL), with the latest public version 1.5 being released in 2017. The French national aerospace research centre (Office National d'Etudes et de Recherches Aéronautiques-ONERA) has also been heavily involved in data-driven modelling, especially in the past 20 years with models that are mostly orbit-specific, such as the International Geostationary Electron model, IGE-2006 (Sicard-Piet et al., 2008) or the low-altitude, proton model OPAL (Boscher et al., 2014), while lately many such local models have been incorporated into a unified, global framework, giving rise to the Global Radiation Earth ENvironment (GREEN) model (Sicard et al., 2018). ESA has also funded the development of a series of models such as the Slot Region Radiation Environment Model (Sandberg et al., 2014), for electrons in the slot region as well as a long series of internal charging models, modelling high energy electrons throughout the magnetosphere with the Flux Model for Internal Charging (FLUMIC), first released in 1998 and last updated in 2003 (Rodgers & Wrenn, 2003), and the Model of Outer Belt Electrons for Dielectric Internal Charging (MOBE-DIC) (Hands et al., 2015) being the most modern such example.

Physics-based models on the other hand, attempt to tackle the kinetic problem of the flow of charged particles within the confines of the Earth's magnetosphere. ONERA's Salammbô model (Beutier & Boscher, 1995; Varotsou et al., 2005, 2008) addresses this by solving the Fokker-Planck diffusion equation in the phase space of the three adiabatic invariants that govern the particle's motion, capturing a wide array of physical processes, such as Coulomb interactions with the plasmasphere electrons, the pitch angle diffusion due to wave-particle interactions and others. Another such model was created by Subbotin and Shprits (2009), called the Versatile Electron Radiation Belt (VERB) code, using a modified-invariants phase space of equatorial pitch angle, energy and  $L^*$ , and employing sophisticated methods to produce the numerical solutions and more detailed interpolation schemes. The British Antarctic Survey radiation belt model (Glauert et al., 2014) also used a similar mathematical formalism, but on a different 3D phase space of pitch angle, energy and  $L^*$ , while the boundary conditions are derived by CRRES/MEA data, grouped by Kp values and averaged, so as to produce different estimates for various geomagnetic activity levels. Nevertheless, the use of Kp-parameterized boundary conditions introduce uncertainties to the prediction of the radiation belt dynamics.

Modelling the SAV modulation (along with other long-term periodic variations) in the particle content of the outer belt has been treated in many ways in the past, but is still a matter of much debate. Models such as IGE-2006 (Sicard-Piet et al., 2008) and MEO-v2 do include a parameterization for the solar cycle phase dependence, but are built on yearly averaged values and are therefore unable to account for shorter scale variations. On the other hand, AE-9 Ginet et al. (2013) offers a particular output type which simulates variations of the mean model outputs, that also include a 6 month periodicity, but this is done from a purely statistical perspective, so there are no means by which to provide inputs to this mode to specify a particular moment in time for such a simulation. Physics-based models such as the British Antarctic Survey radiation belt model (Glauert et al., 2014) and the Salammbô model (Beutier & Boscher, 1995; Varotsou et al., 2005, 2008) typically rely on some index or parameter of magnetospheric activity (e.g. Kp, magnetopause radial distance etc.) to estimate the acceleration due to wave-particle interactions and thus predict the changes in electron phase space density, and so is not clear how or if they take SAV-and other large scale variations-into account. Finally, machine learning models such as the recent MERLIN model (Smirnov et al., 2020) or the Non-linear AutoRegressive Moving Average with exogenous inputs (NARMAX) models (Boynton et al., 2019, 2020), built on many years of data, probably include the effects of all such

variabilities, but in a way that is difficult to disentangle from all the other effects and variations.

This study aims in incorporating the recent findings concerning the SAV in the relativistic electron fluxes of the outer radiation belt in order to develop a model which can accurately reproduce this long-term modulation and coupling it with solar wind parameters as inputs to derive accurate predictions. The rest of the paper is organized as follows: section 2 describes the data selection and the pre-processing analysis applied in the data, section 3 describes the investigation and building of the model, and the results in the various energy channels of RBSP/MagEIS and L-shells and section 4 is dedicated to the validation of the model and discussion of the results.

## 2 Datasets

In this study we make use of the 11-sec resolution spin-averaged differential fluxes (Level 2–Release 4) from the Magnetic Electron Ion Spectrometer (Blake et al., 2013) on board the Radiation Belt Storm Probes (RBSP). The dataset used spans the 0.033–4.062 MeV range and use data during the September 2013 up to July 2019 time period from both RBSP-A and B. We do not use data prior to September 2013 due to MagEIS having had several major changes to energy channel definitions, operational modes, and flux conversion factors over the early part of the mission (Boyd et al., 2019). Specifically we use the background corrected data (Claudepierre et al., 2015) considering measurements where the background correction error is less than 75%. Finally, we apply the correction factors proposed by Sandberg et al. (2021).

We also analyze electron integral flux measurements with energies  $>0.8$  MeV from the Energetic Proton, Electron and Alpha Detector (EPEAD–<https://satdat.ngdc.noaa.gov/sem/goes/data/>) on board the GOES-15 spacecraft (Onsager et al. (1996) and GOES N Series Data Book, 2010), spanning the 2012–2018 time-period. Following Baker, Zhao, et al. (2019), we use data only from the GOES-15 "East" sensor since the "West" sensor often exhibits on-orbit degradation.

The dataset further includes 1-min resolution measurements of the solar wind speed and dynamic pressure, as well as 1-hour measurements of Solar flux at 10.7 cm available by the OMNIWeb service of the Space Physics Data Facility at the Goddard Space Flight Center (<http://omniweb.gsfc.nasa.gov/>).

For the calculation of the  $\theta$  angle (which corresponds to the tilt of the Earth's dipole axis with respect to the heliographic equatorial plane), we use the International Radiation Belt Environment Modelling (IRBEM) library ("International Radiation Belt Environment Modelling Library", 2009). Finally, the L-shell values are obtained from the magnetic ephemeris files of the ECT Suite (<https://www.rbsep-ect.lanl.gov/science/DataDirectories.php/>), which are calculated using the Tsyganenko (2005) magnetospheric field model (TS05).

## 3 Investigation of electron reproduction with multivariate regression

### 3.1 Physical parameters and mathematical/physical formulation

For the performed analysis, the spin-averaged differential electron fluxes with equatorial pitch angles greater than 75 degrees are grouped into daily bins in time and with  $dL=0.2$  at L-shell resulting in a dataset of more than  $\approx 530000$  data points (excluding data gaps, NaN values, e.t.c.), from the  $\approx 2100$  daily bins, at 17 L-shell bins, for 18 electrons energies each. We note that we use in our analysis the 2.5–5.9 L-shell range. This effectively includes the slot region and the major part of the outer belt except for the GEO environment. The same daily binning in time is applied for the Solar wind speed, dynamic pressure, Solar flux at 10.7 cm and the  $\theta_{RM}$  angle. Then a 30-days moving average is calculated in order to exclude variations due to the Solar rotation. Using the fi-



nal dataset we perform an initial investigation using a multiple regression scheme with the mathematical formulation shown below (equation 1).

$$J = e^{c_1 \cdot s\Theta + c_2 \cdot c\Theta + c_0} \cdot P_{SW}^{\alpha_1 + \beta_1 \cdot \ln(P_{SW})} \cdot V_{SW}^{\alpha_2 + \beta_2 \cdot \ln(V_{SW})} \cdot SF^{\alpha_3 + \beta_3 \cdot \ln(SF)} \quad (1)$$

Where SF is the Solar flux at 10.7 cm and  $V_{SW}$  and  $P_{SW}$  is the Solar wind speed and dynamic pressure, respectively.  $s\Theta$  and  $c\Theta$  correspond to the sine and cosine of the angle that controls the Russell-McPherron effect (Russell & McPherron, 1973), respectively, in the following form:  $s\Theta = \sin(\theta_{RM}/2)$  and  $c\Theta = \cos(\theta_{RM}/2)$ .

The approach in the aforementioned formulation is congruent with Katsavrias, Aminalragia-Giamini, et al. (2021) as it is the product of power laws of the three variables but with added feedback terms in the power index - in the form of the natural logarithm of the variables themselves. This essentially creates a product of variable power laws which is in the same spirit with existing universal coupling functions such as the Newell function or the Epsilon parameter (Newell et al., 2007). Finally, we must emphasize the use of the modifying factor which contains the  $\theta_{RM}$  angle dependence, which as shown by Katsavrias, Papadimitriou, et al. (2021) is crucial for capturing the long-term modulation (SAV).

From a physics point of view, the magnitude of the electron flux in the outer radiation belt is expressed as a combination of solar wind speed and pressure along with the intensity of the cycle in terms of the Solar flux at 10.7 cm, which are indirectly linked with the two major drivers of geospace disturbances; the Interplanetary Coronal Mass Ejections (ICMEs) and the High Speed Streams (HSS). The reasoning behind the selection of these input parameters is based on the results of Katsavrias, Papadimitriou, et al. (2021) who showed that the semi-annual variation in the relativistic electron fluxes of the outer radiation belt was more pronounced during periods of increased (decreased) number of HSS (ICME) occurrence indicating that the SAV is the result of the modulation of reconnection produced by the variability of the controlling angle of the RM mechanism during periods of enhanced solar wind speed and decreased Solar cycle intensity. The latter is in agreement with X. Li et al. (2001) who indicated the anti-correlation of the outer edge of the outer belt with the sunspot number which leads consequently to variability due to various drivers since ICMEs prevail during the solar maximum and HSSs during the descending phase.

### 3.2 Results

Figure 1 presents the results of the multiple regression for the 0.346 and 0.909 MeV electron fluxes from MagEIS during the 2013–2019 time-period at  $L=4.6$  ( $4.5 < L \leq 4.7$ ) and 5.2 ( $5.1 < L \leq 5.3$ ), respectively. As shown the regression is quite accurately reproduces the electron fluxes (panels a and c) at both selected energy channels and L-shells, with the Pearson’s correlation coefficient being 0.831 and 0.854 for the 0.346 and 0.909 MeV, respectively, while the mean absolute percentage error (MAPE) is 48.81 and 26.83%, respectively.

In detail, the regression accurately reproduces both the high and low flux values during the late maximum and the descending phase of the solar cycle 24 (SC24), especially during 2015 up to 2017. Nevertheless, the lowest flux values are overestimated during the minimum phase (2018–2019). We note that despite this overestimation of the lower flux values, the evident semi-annual variation during the whole time-period under investigation is reproduced very well. The latter highlights the importance of using the  $\theta_{RM}$  as an input parameter. Furthermore, the vast majority of the regressed values fall within a factor of two of the data, represented by the two green solid lines (panels b and d), and mostly cluster along the equality line in blue for both the selected energy channels and L-shells. Especially for the 0.346 MeV (1b), the regression seems to overestimate a sig-

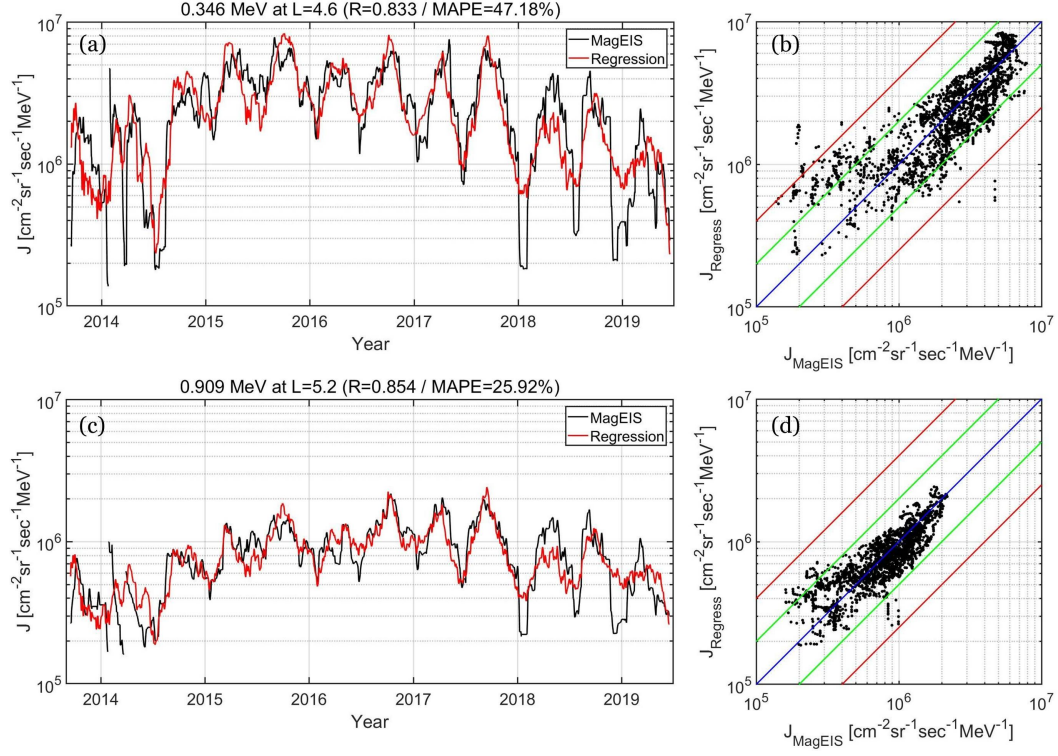


**Figure 1.** Examples of the multiple regression. Panels a and c: 30-days running averages of spin-averaged electron fluxes for 0.346 MeV at L=4.6 and 0.909 MeV at L=5.2, respectively. Black and red solid lines correspond to the measured and regressed time-series, respectively. Panels b and d: Cross-plots between the measured and regress electron fluxes. The solid blue line corresponds to  $y=x$  and the solid green lines correspond to  $y=2\cdot x$  and  $y=x/2$ . The solid red lines correspond to  $y=4\cdot x$  and  $y=x/4$ . Dataset spans the whole 2013–2019 time-period. The free parameters for the regression of the 0.346 MeV at L=4.6 are:  $c_0=-402.79$ ,  $c_1=-0.004$ ,  $c_2=-38.54$ ,  $\alpha_1=3.68$ ,  $\beta_1=-1.95$ ,  $\alpha_2=118.52$ ,  $\beta_2=-9.45$ ,  $\alpha_3=35.07$ ,  $\beta_3=-3.71$  and the corresponding correlation coefficient and mean absolute percentage error are 0.833 and 47.18%, respectively. The free parameters for the regression of the 0.909 MeV at L=5.2 are:  $c_0=-32.98$ ,  $c_1=-0.20$ ,  $c_2=-21.50$ ,  $\alpha_1=2.27$ ,  $\beta_1=-1.48$ ,  $\alpha_2=4.41$ ,  $\beta_2=-0.07$ ,  $\alpha_3=18.67$ ,  $\beta_3=-2.04$  and the corresponding correlation coefficient and mean absolute percentage error are 0.854 and 25.92%, respectively.

216 nificant fraction of the lower flux values ( $< 10^6 \text{ cm}^{-2} \text{ sec}^{-1} \text{ sr}^{-1} \text{ MeV}^{-1}$ ) which, never-  
 217 theless, fall within a factor of four of the measured fluxes (red solid lines). This feature  
 218 is significantly less prominent in the 0.909 MeV (1d) electron fluxes, indicating that it  
 219 may be both L and energy dependent.

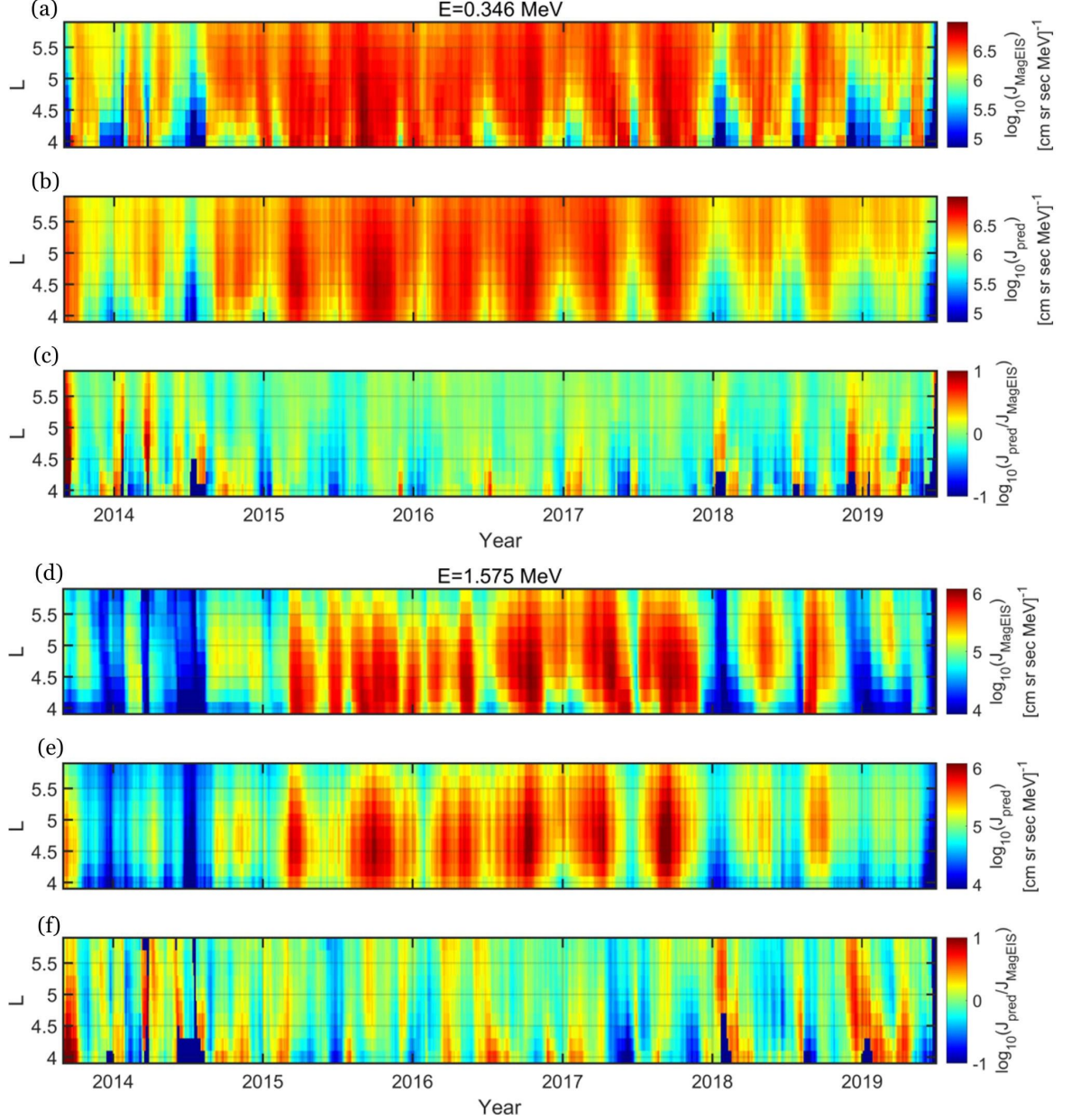


**Figure 2.** Flux maps of the 30-days running averages of daily flux at  $L > 4$  as a function of L-shell for two energy channels at 0.346 and 1.575 MeV, respectively. Panels a and d correspond to the MagEIS measured fluxes, panels b and e correspond to the regressed fluxes and panels c and f to their ratio.

220 In order to provide a more detailed comparison between the regressed and measured  
 221 fluxes as a function of L-shell, figure 2 shows the flux maps of the 30-days running  
 222 averages of daily flux as a function of L-shell for the 0.346 and 1.575 MeV energy chan-

nels of MagEIS. We note that the regression of each energy channel is done separately for each L-shell bin. Panels a and d, show the MagEIS measured fluxes for the two energy channels, while panels b and e show the corresponding regressed values. Panels c and f show the ratio of the regressed over the measured fluxes with the red (blue) color indicating that the model overestimates (underestimates) the true flux values. As shown the regression can successfully reproduce the electron fluxes for both sub-relativistic (0.346 MeV) and relativistic electrons (1.575 MeV) throughout the whole time-period and at all  $L > 4$ .

In detail, the model can reproduce the measured electron fluxes in the heart of the outer radiation belt and especially the intense activity during the descending phase of SC24 (2015–2017). It is worth mentioning that this intense activity during the descending phase of the Solar cycle coincides with pronounced semi-annual variation and high occurrence of High Speed Streams (Katsavrias, Papadimitriou, et al., 2021), indicating the crucial role of the SAV during periods of enhanced solar wind speed and decreased Solar cycle intensity. Furthermore, as shown in panels c and f, the model overestimates the lowest electron flux values, especially during 2014 (Solar maximum) and 2019 (late minimum of SC24). We note that this feature is also present in figure 1 and here we show that it is dependent on the electron energy, namely, the disagreement between the regressed and measured electron fluxes is larger for increasing energy and for decreasing L-shell values.

## 4 Machine learning model

### 4.1 Machine learning model structure

The regression scheme described in the previous section is very useful in the investigation of the reproduction of the electron fluxes as well as the influence of each solar variable. Nevertheless, in practice and for the construction of a model such an approach would require separate regressions for each combination of energy and L-shell and furthermore does not necessarily perform well when used in a predictive manner, i.e. when presented with inputs not used in the derivation of the free parameters. In addition, with such an approach it would not be trivial to extend or even interpolate fluxes for L values not used in the regression. Equation 1 can be re-written in logarithmic form as in equation 2 below, which more clearly shows the separate inputs. They consist of the intercept and 8 terms, which are the logarithms of the three solar parameters, Solar wind speed, dynamic pressure and Solar flux at 10.7 cm, along with their respective squares and the two terms of the Russell-McPherron angle.

$$\ln(J) = c_0 + c_1 \cdot s\Theta + c_2 \cdot c\Theta + \alpha_1 \cdot \ln(P_{sw}) + \beta_1 \cdot \ln(P_{sw})^2 + \alpha_2 \cdot \ln(V_{sw}) + \beta_2 \cdot \ln(V_{sw})^2 + \alpha_3 \cdot \ln(SF) + \beta_3 \cdot \ln(SF)^2 \quad (2)$$

Moreover, we use similar binning process with the one described in section 3.1, except that here we infer two distribution components. In detail, the spin-averaged differential electron fluxes with equatorial pitch angles greater than 75 degrees are grouped into daily bins in time and with  $dL=0.2$  at L-shell. From these bins we infer the mean and the 95th quantile (henceforward Q95) of the fluxes. At the same extent, from the daily binning of the Solar/solar wind parameters we infer the same distribution components (mean and Q95). Then a 30-days moving average is calculated, both for the mean and the Q95, using a window that includes the current timestamp and 29 days prior.

In order to create a robust model that is parametric with respect to the L-shell value, as well as having good predictive capabilities, as is shown further on, we use neural networks. The 8 parameter terms along with the L value are used as input, and the model outputs electron fluxes at all 18 energies simultaneously. The neural networks are mul-



tilayer feed-forward nets with three hidden layers using the hyperbolic tangent sigmoid transfer function and 18 outputs which correspond to the logarithms of the electron fluxes for the 18 MagEIS energies. We use a parallel array of three nets where the individual outputs are averaged before the final output is derived.

This modelling approach has three significant benefits. First, the spectral coherency of the electron fluxes across the wide electron energy range is maintained as they are one consistent output. Second, the model is able to generalize with respect to the L-shell and output fluxes for arbitrary L values even outside the range with which it was trained with, as is shown further on. Finally it is possible to use the model in a predictive capability, i.e. train it with a fraction of the data and test its performance with the remaining data at all energies and L values. In this regard we have used a 60-40 division where 1250 of the  $\approx 2100$  daily values are randomly selected and used to train the neural networks whereas the remaining  $\approx 900$  daily values are used to evaluate the performance of the model. We note that each daily bin contains electron fluxes for all L-shells and energies, barring data gaps. Therefore the actual flux data points used for training amount to  $\approx 310000$  and those for testing to  $\approx 220000$  which are more than adequate dataset sizes for training and testing such a machine learning approach.

Finally we note an important aspect taken into account for the evaluation of the model's predictive capability shown in the results. It is a moot point to predict daily electron fluxes using the values of the solar parameters from the same day; as discussed for each day, we use the moving average of the 29 days prior and the current one, for both the fluxes and the solar parameters. However, we train and test the model to use the input variables of the previous day for the prediction of the electron fluxes, i.e. there is a consistent time-shift of one day between predictor and outcome, as it would be necessary in an operational manner.

## 4.2 Model performance and prediction results

Figure 3 shows comparisons of the data fluxes and the predictions of the model for the test dataset at four L-shells and at all electron energies of the MagEIS instrument. As seen, the model can accurately predict the electron fluxes in the whole energy range with the vast majority of points clustering along the equality line and differing no more than a factor of two. We note that the model can accurately predict the electron fluxes even in the slot region (panel a) despite the fact that there are much less data points at the higher electron energies, this is a strong indication of good generalization of the NNs both in L and energy. The presence of high energy electrons in the slot region is attributed at the few intense events, during SC24, which filled this region with relativistic electrons. At L=3.6 (panel b) we have a significantly increased amount of data points. The model has a remarkable accuracy at the lower energy channels (source electrons at  $E < 100$  keV) with the data points clustering along the equality line and the spread being much less than a factor of two. The higher energies ( $> 1$  MeV) are also accurately predicted, while at intermediate energies there are some outliers which exceed the factor of two. However, considering the total number of data points, the outliers represent a small fraction. Also it is worth noting that there is no discernible trend in the amount of points which overestimate/underestimate the measured electron fluxes. At the heart of the outer radiation belt (panels c and d at L=4.6 and 5.6, respectively), the vast majority of the predicted fluxes are clustered along the equality line differing no more than a factor of two. Finally, at L=5.6 (panel d) there is an observed underestimation of the higher flux values of the 0.033 and 0.054 MeV electron fluxes, which, nevertheless, is again mostly within a factor of two.

The Q95 component of the distribution (figure 4) exhibit very similar behaviour. Once again, the vast majority of the predicted fluxes are clustered along the equality line differing no more than a factor of two at all L-shells. Nevertheless, there are the same

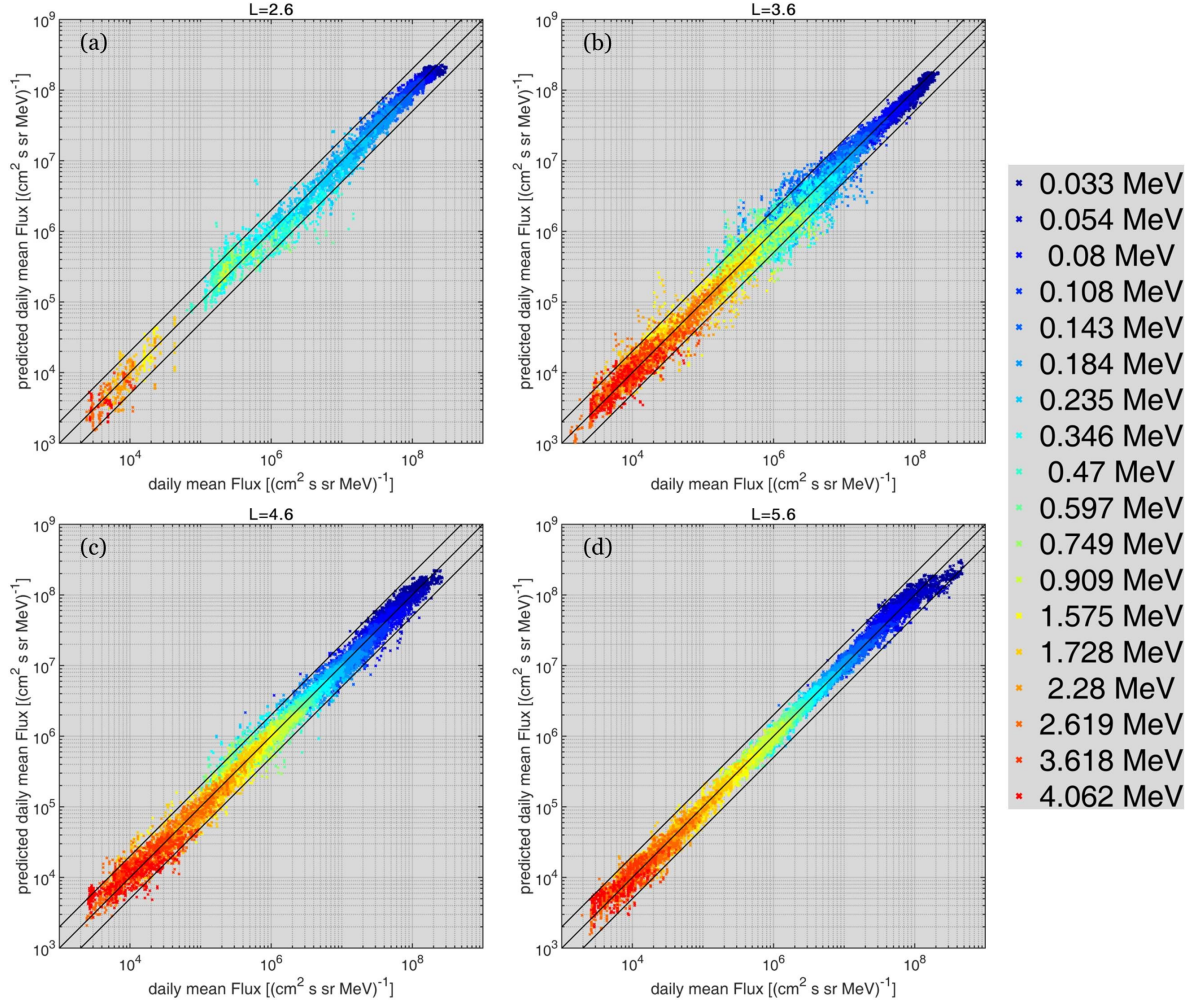


**Figure 3.** Cross-plots of the predicted daily mean of the flux values over the measured ones for four L-shell values at (a) 2.6, (b) 3.6, (c) 4.6 and (d) 5.6. The energy channels are color-coded with red (blue) corresponding to the higher (lower) MagEIS energies. The black solid lines correspond to the equality line and to  $y=2 \cdot x$  and  $y=x/2$ , respectively.

two deviations observed also in the mean component. At  $L=3.6$  (panel b), the intermediate energies (235–749 keV) contain some outliers which exceed the factor of two, even though once again, the outliers represent a small fraction of the total number of data points, while at  $L=5.6$  (panel d) there is again a small underestimation of the higher flux values of the 0.033 and 0.054 MeV electron fluxes, which, nevertheless, is again mostly within a factor of two.

Figure 5 shows the occurrence density plot of the predicted versus the observed flux for all energies and all L-shells. The left panel corresponds to the daily mean and the right panel to the daily Q95 of the electron fluxes. The solid red line is the equality line and the solid white are the factor-of-two lines,  $y=2x$  and  $y=x/2$ . As shown, the occurrence maxima (red color) exhibit a remarkable agreement in both distribution components, following the equality line and the vast majority of the data points are within the factor of two from it.



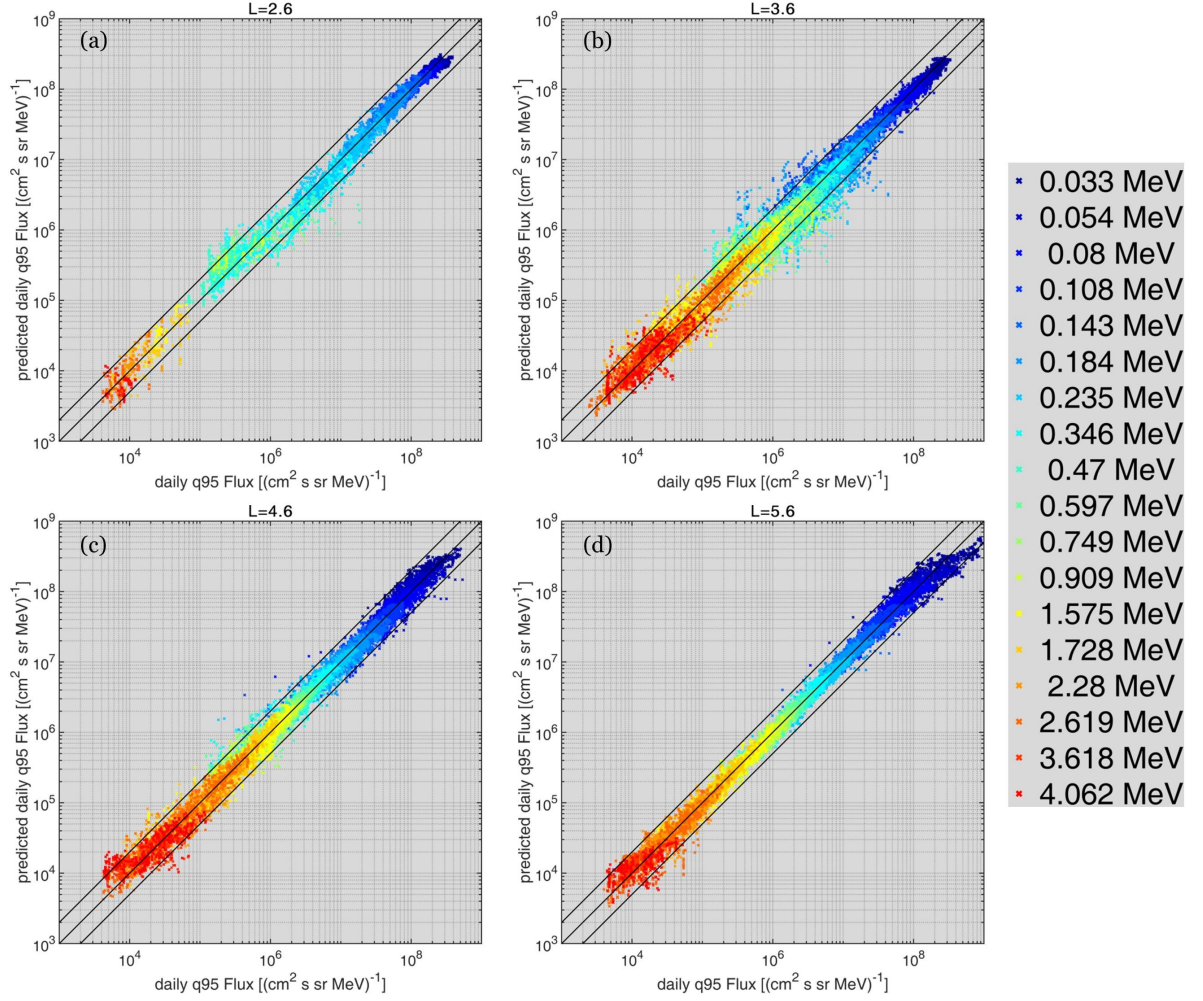


**Figure 4.** Same with figure 3 but for the predicted daily Q95 of the flux values.

Furthermore, figure 6 shows the distribution of the Mean Absolute Percentage Error (MAPE—left panels) and the percentage of points within a factor of two (Ratio 2—right panels) as a function of electron energy and L-shell, with blue (red) corresponding to the lower (higher) MAPE and Ratio 2 values. Top panels (a and b) correspond to the mean electron fluxes, while bottom panels (c and d) to the Q95.

For the mean fluxes, the overall MAPE is at most 50% and the Ratio 2 at 75% at its absolute minimum with most values being significantly lower and higher, respectively. This highlights the successful performance of the model across all L values and energies. For  $L > 4$  virtually all energy channels have MAPE values less than 30% and Ratio 2 values more than 95% in agreement with what was shown in figure 3. For  $L < 4$  (slot region and the inner boundary of the outer belt) there are two distinct islets that exhibit comparatively increased MAPE and decreased Ratio 2 values. The first islet is roughly located at  $2.6 < L < 3.6$  in the  $0.2 < E < 0.9$  MeV energy range, while the second smaller islet is roughly located at  $2.8 < L < 3.2$  in the  $1.3 < E < 2$  MeV energy range. The highest MAPE of 50% is found here, as well as the lowest Ratio 2 percentage of 75%. This is consistent with the results shown in figure 3b. A possible explanation for this is the low occurrence of electrons with relativistic energies at such low L-shells since there were

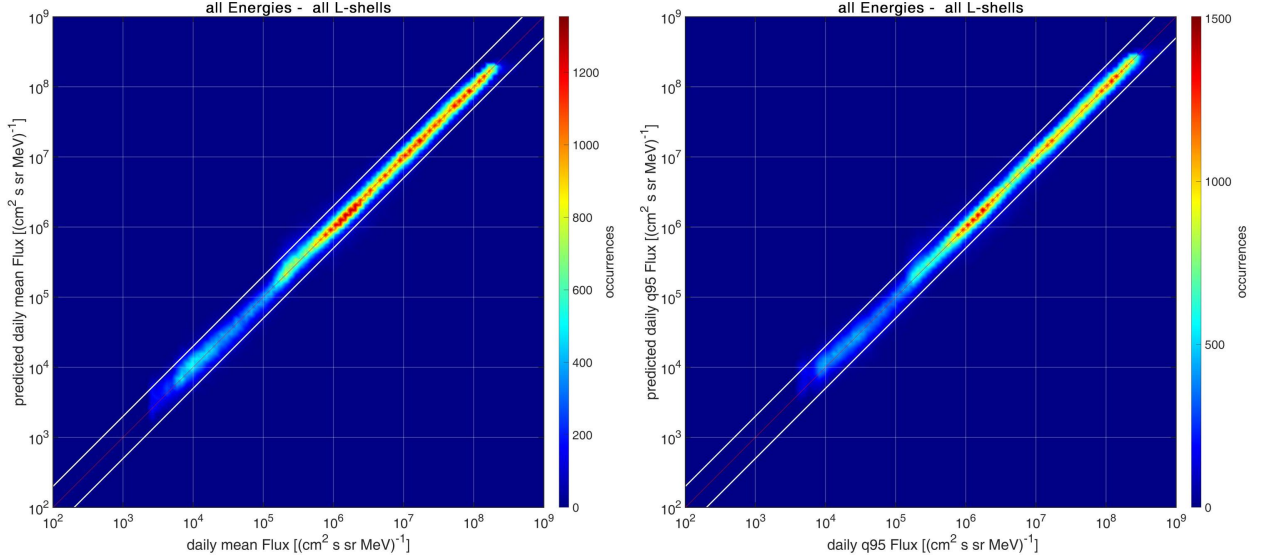


**Figure 5.** Density plot of the predicted daily mean (left panel) and daily Q95 (right panel) flux values and the measured ones for the complete dataset at all L-shells and all energies. Solid black line corresponds to the one-to-one relationship between observations and predictions, while the solid white lines correspond to  $y=2 \cdot x$  and  $y=x/2$ .

very few intense events during SC24, which were capable of penetrating so deep in the inner magnetosphere (Baker, Hoxie, et al., 2019).

Concerning the Q95 fluxes, a remarkably similar trend is observed. Once again, at  $L > 4$ , all energy channels have MAPE values less than 30% and Ratio 2 values more than 95%, while at  $L < 4$  there are the same two distinct islets—located at the same L-shell and energy range—that exhibit comparatively increased MAPE and decreased Ratio 2 values. The only difference compared to the mean fluxes is that the highest MAPE of the Q95 is 60% (470–597 keV at  $L \approx 2.8$ ), while the lowest Ratio 2 percentage is 70% (346–597 keV at  $2.8 < L < 3.2$ ).

### 4.3 Extension and Validation at GEO

In the previous sections we have investigated and tested the regression and prediction capabilities of electron fluxes in the outer belt using solar parameters as drivers. Nevertheless, the results shown were within the time-span and L-shell range provided by the MagEIS instrument on board the RBSP satellites. In order to test the generalization and prediction capabilities of our model outside this temporal and spatial range we use the omni-directional integral fluxes at  $E > 0.8$  MeV provided by the EPEAD instrument on board GOES-15 during the 2012–2018 time period covering the maximum and descending phase of SC24. We use the model to derive differential fluxes using an input of  $L=6.65$  ( $\pm 0.05$ ), which corresponds to the average L-shell location of GOES-15 during the aforementioned time period. Also, the data from January 2012 to August 2013 are completely outside the temporal range of the training dataset, meaning they are completely unknown to the model. This offers an opportunity for a robust validation of the performance of the model in spatio-temporal dimensions. From the predicted differential fluxes the  $E > 0.8$  MeV integral fluxes are calculated. We note that the GOES/EPEAD time-series are also grouped in daily bins and a moving average using a window that contains the current time-stamp and 29 before is used.

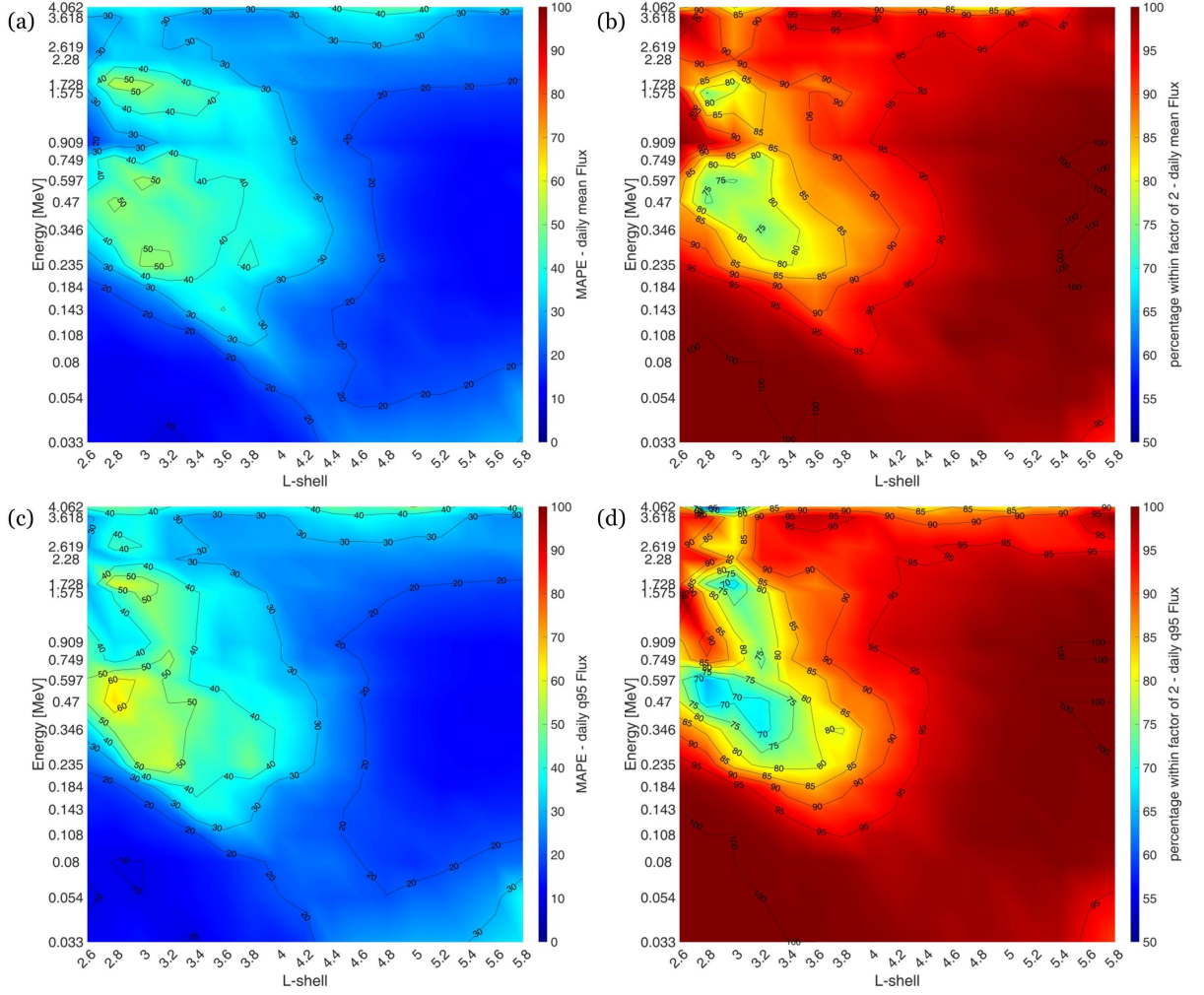


**Figure 6.** Distribution of the Mean Absolute Percentage Error (MAPE—panel a) and the percentage of points within a factor of two (Ratio 2—panel b) as a function of electron energy and L-shell for the daily mean of the electron fluxes. Same for the daily Q95 at panels c and d.

Figure 7a shows the comparison of the 30-days running averages of the daily mean of the integral electron fluxes for  $E > 0.8$  MeV at GEO (black solid line) with the predicted fluxes inferred from our model (red dashed line). As shown, there is a very good agreement between the predicted and the measured integral fluxes especially during the descending phase of SC24, while the model overestimates the lowest flux values ( $< 10^4 \text{ cm}^2 \text{ sec}^{-1} \text{ sr}^{-1}$ ) during the maximum (2013–2014) and the minimum (2018) of SC24.

However, as shown in figure 7b, the large majority of the predicted electron fluxes differ no more than a factor of two from the measured ones, with the corresponding MAPE and Ratio 2 being 37.31% and 89.85%, respectively. We note, that the predicted flux data shown are adjusted by a factor of 3.74 in order to achieve the observed agreement in both panels. This is consistent and well within the range shown by Baker, Zhao, et al. (2019) who reported that the EPEAD fluxes differ from MagEIS by a factor of one to ten at  $L = 6.6 \pm 0.05$ . These results further demonstrate and validate the predictive capability of our model even for inputs it has not been trained with.



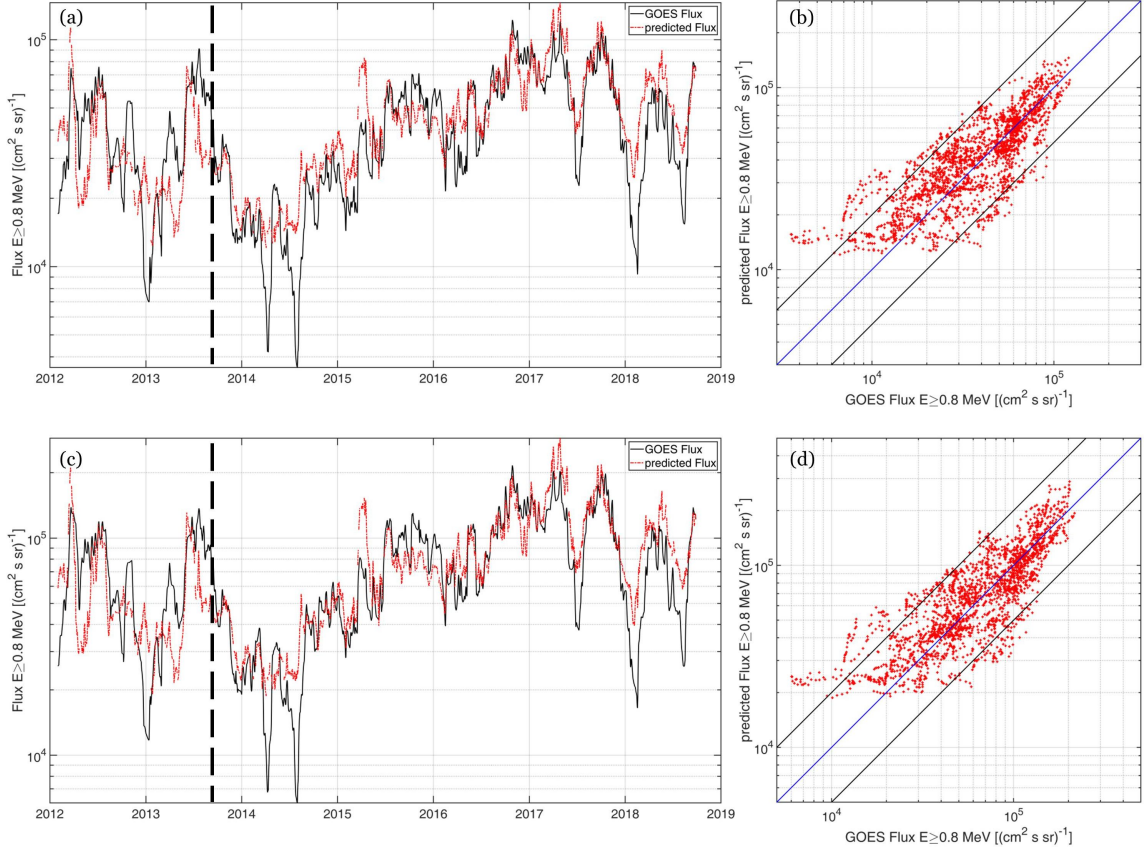


**Figure 7.** Panel a: 30-days running averages of daily mean integral electron fluxes for  $E > 0.8$  MeV at GEO from GOES-15/EPEAD during 2012–2018 time period. The black solid line corresponds to the measured integral fluxes. The red dashed line corresponds to the predicted time-series inferred from the integration of the 0.8–4 MeV differential electron flux from MagEIS with Ratio 2 and the corresponding mean absolute percentage error being 89.85% and 37.31%, respectively. Panel b: Cross-plot of the predicted versus the measured 30-days running averages of daily mean integral electron fluxes at  $E > 0.8$  MeV. Panels c and d are similar with a and d, respectively, but for the 30-days running averages of daily Q95 integral electron fluxes at  $E > 0.8$  MeV. Ratio 2 and the corresponding mean absolute percentage error being 89.58% and 34.99%, respectively. The black dashed lines mark the September 1<sup>st</sup>, 2013 which corresponds to the date of the first measurement of RBSP/MagEIS used to train the model.

Similar results are observed for the Q95 component (panels c and d) with the corresponding MAPE and Ratio 2 being 34.99% and 89.58%, respectively. Once again, there is a small overestimation of the lowest Q95 flux values ( $< 10^4 \text{ cm}^2 \text{ sec}^{-1} \text{ sr}^{-1}$ ) during the maximum (2013–2014) and the minimum (2018) of SC24. Nevertheless, the model successfully predicts the highest Q95 flux values which fall within the equality line (panel d).

Finally, it must be emphasized that the model successfully provides prediction of the 30-day running averages of GOES fluxes (both for the mean and the Q95 daily values) even before the September 1<sup>st</sup> of 2013 accounting for a time-period of 20 months (see the vertical dashed lines in figure 7), which as discussed above, are completely out-of-sample. This means that the model is able to predict the electron fluxes simultane-

ously outside the L-shell training scheme and outside the time interval used for the training.

## 5 Conclusions

We have used almost 7 years (2013–2019) of RBSP/MagEIS measurements of electron fluxes in the outer radiation belt—which is one of the most reliable electron flux datasets—to develop a model which can successfully predict the time-series of the 30-day averages (in terms of mean and Q95 values) of electron fluxes in the 0.033–4.062 MeV energy range and in the 2.5–5.9 L-shell range.

The model is based on a simple mathematical formulation that echoes already existing coupling functions such as the Newell function or the Epsilon parameter, using a product of variable power laws of solar wind speed, dynamic pressure and Solar flux at 10.7 cm. Moreover, it includes a constant containing the  $\theta_{RM}$  angle, which controls the Russell-McPherron effect and which we showed to be crucial for accurately predicting both the intensity and the modulation of radiation belt fluxes, especially during the descending phase of SC24, where the highest intensities occur. Moreover, we have used comparisons with the GOES-15/EPEAD integral fluxes at GEO to demonstrate that the model can successfully predict electron fluxes even outside the training scheme - both temporally and spatially. Thus, the model provides accurate time-series of the electron flux distribution in the outer belt, over long time-periods and over a broad electron energy range without being constraint by the L-shell range of the training dataset.

In addition, since it is driven by parameters which are available in near-real time, it has also the potential to be used as an operational model for nowcasting/forecasting electron fluxes, which we showcase by using the 1-day time-shift. Furthermore, it can be used in conjunction with other models/methodologies, which have a shorter forecasting horizon, e.g. Katsavrias, Aminalragia-Giamini, et al. (2021), in order to derive even more detailed daily predictions. Its applicability also extends to the provision of reliable predictions of the boundary conditions in physics-based models.

## Acknowledgments

This work has received funding from the European Union’s Horizon 2020 research and innovation programme ”SafeSpace” under grant agreement No 870437 and from the European Space Agency under the ”European Contribution to International Radiation Environment Near Earth (IRENE) Modelling System” activity under ESA Contract No 4000127282/19/NL/IB/gg. The authors acknowledge Bern Blake, Joe Fennell, Seth Claudepierre, and Drew Turner for the use of MagEIS data which can be found online in <https://www.rbsp-ect.lanl.gov/science/DataDirectories.php>. The authors also acknowledge GOES-15/EPEAD team and the developers of the International Radiation Belt Environment Modeling (IRBEM) library that was used to calculate the theoretical angle of the Russell-McPherron mechanism.

## References

- Baker, D. N., Hoxie, V., Zhao, H., Jaynes, A. N., Kanekal, S., Li, X., & Elkington, S. (2019, April). Multiyear measurements of radiation belt electrons: Acceleration, transport, and loss. *Journal of Geophysical Research: Space Physics*, 124(4), 2588–2602. Retrieved from <https://doi.org/10.1029/2018ja026259> doi: 10.1029/2018ja026259
- Baker, D. N., Kanekal, S. G., Pulkkinen, T. I., & Blake, J. B. (1999, October). Equinoctial and solstitial averages of magnetospheric relativistic electrons: A strong semiannual modulation. *Geophysical Research Letters*, 26(20), 3193–3196. Retrieved from <https://doi.org/10.1029/1999gl1003638> doi:

- 10.1029/1999gl003638
- Baker, D. N., Zhao, H., Li, X., Kanekal, S. G., Jaynes, A. N., Kress, B. T., . . .  
Hoxie, V. (2019, December). Comparison of van allen probes energetic electron data with corresponding GOES-15 measurements: 2012–2018. *Journal of Geophysical Research: Space Physics*, 124(12), 9924–9942. Retrieved from <https://doi.org/10.1029/2019ja027331> doi: 10.1029/2019ja027331
- Beutier, T., & Boscher, D. (1995). A three-dimensional analysis of the electron radiation belt by the salammbô code. *Journal of Geophysical Research: Space Physics*, 100, 14853. doi: 10.1029/94JA030661995
- Blake, J. B., Carranza, P. A., Claudepierre, S. G., Clemmons, J. H., Crain, W. R., Dotan, Y., . . . Zakrzewski, M. P. (2013, June). The magnetic electron ion spectrometer (MagEIS) instruments aboard the radiation belt storm probes (RBSP) spacecraft. *Space Science Reviews*, 179(1-4), 383–421. Retrieved from <https://doi.org/10.1007/s11214-013-9991-8> doi: 10.1007/s11214-013-9991-8
- Boscher, D., Sicard-Piet, A., Lazaro, D., Cayton, T., & Rolland, G. (2014, December). A new proton model for low altitude high energy specification. *IEEE Transactions on Nuclear Science*, 61(6), 3401–3407. Retrieved from <https://doi.org/10.1109/tns.2014.2365214> doi: 10.1109/tns.2014.2365214
- Boyd, A. J., Reeves, G. D., Spence, H. E., Funsten, H. O., Larsen, B. A., Skoug, R. M., . . . Jaynes, A. N. (2019, November). RBSP-ECT combined spin-averaged electron flux data product. *Journal of Geophysical Research: Space Physics*, 124(11), 9124–9136. Retrieved from <https://doi.org/10.1029/2019ja026733> doi: 10.1029/2019ja026733
- Boynton, R. J., Amariutei, O. A., Shprits, Y. Y., & Balikhin, M. A. (2019, June). The system science development of local time-dependent 40-keV electron flux models for geostationary orbit. *Space Weather*, 17(6), 894–906. Retrieved from <https://doi.org/10.1029/2018sw002128> doi: 10.1029/2018sw002128
- Boynton, R. J., Aryan, H., Dimmock, A. P., & Balikhin, M. A. (2020, November). System identification of local time electron fluencies at geostationary orbit. *Journal of Geophysical Research: Space Physics*, 125(11). Retrieved from <https://doi.org/10.1029/2020ja028262> doi: 10.1029/2020ja028262
- Claudepierre, S. G., O'Brien, T. P., Blake, J. B., Fennell, J. F., Roeder, J. L., Clemmons, J. H., . . . Larsen, B. A. (2015, July). A background correction algorithm for van allen probes MagEIS electron flux measurements. *Journal of Geophysical Research: Space Physics*, 120(7), 5703–5727. Retrieved from <https://doi.org/10.1002/2015ja021171> doi: 10.1002/2015ja021171
- Daglis, I. A., Katsavrias, C., & Georgiou, M. (2019, May). From solar sneezing to killer electrons: outer radiation belt response to solar eruptions. *Philosophical Transactions of the Royal Society A: Mathematical, Physical and Engineering Sciences*, 377(2148), 20180097. Retrieved from <https://doi.org/10.1098/rsta.2018.0097> doi: 10.1098/rsta.2018.0097
- Ginet, G. P., O'Brien, T. P., Huston, S. L., Johnston, W. R., Guild, T. B., Friedel, R., . . . Su, Y.-J. (2013, March). AE9, AP9 and SPM: New models for specifying the trapped energetic particle and space plasma environment. *Space Science Reviews*, 179(1-4), 579–615. Retrieved from <https://doi.org/10.1007/s11214-013-9964-y> doi: 10.1007/s11214-013-9964-y
- Glauert, S. A., Horne, R. B., & Meredith, N. P. (2014, January). Three-dimensional electron radiation belt simulations using the BAS radiation belt model with new diffusion models for chorus, plasmaspheric hiss, and lightning-generated whistlers. *Journal of Geophysical Research: Space Physics*, 119(1), 268–289. Retrieved from <https://doi.org/10.1002/2013ja019281> doi: 10.1002/2013ja019281
- Hands, A., Ryden, K., Underwood, C., Rodgers, D., & Evans, H. (2015, December). A new model of outer belt electrons for dielectric internal charg-



- ing (MOBE-DIC). *IEEE Transactions on Nuclear Science*, 62(6), 2767–2775. Retrieved from <https://doi.org/10.1109/tns.2015.2475134> doi: 10.1109/tns.2015.2475134
- International radiation belt environment modelling library. (2009, April). *Space Research Today*, 174, 27–28. Retrieved from <https://doi.org/10.1016/j.srt.2009.03.006> doi: 10.1016/j.srt.2009.03.006
- Jaynes, A. N., Baker, D. N., Singer, H. J., Rodriguez, J. V., Lotoaniu, T. M., Ali, A. F., ... Reeves, G. D. (2015, September). Source and seed populations for relativistic electrons: Their roles in radiation belt changes. *Journal of Geophysical Research: Space Physics*, 120(9), 7240–7254. Retrieved from <https://doi.org/10.1002/2015ja021234> doi: 10.1002/2015ja021234
- Katsavrias, C., Aminalragia-Giamini, S., Papadimitriou, C., Sandberg, I., Jiggins, P., Daglis, I., & Evans, H. (2021, May). On the interplanetary parameter schemes which drive the variability of the source/seed electron population at GEO. *Journal of Geophysical Research: Space Physics*, 126(6). Retrieved from <https://doi.org/10.1029/2020ja028939> doi: 10.1029/2020ja028939
- Katsavrias, C., Daglis, I. A., & Li, W. (2019, April). On the statistics of acceleration and loss of relativistic electrons in the outer radiation belt: A superposed epoch analysis. *Journal of Geophysical Research: Space Physics*. Retrieved from <https://doi.org/10.1029/2019ja026569> doi: 10.1029/2019ja026569
- Katsavrias, C., Papadimitriou, C., Aminalragia-Giamini, S., Daglis, I. A., Sandberg, I., & Jiggins, P. (2021, May). On the semi-annual variation of relativistic electrons in the outer radiation belt. *Annales Geophysicae*, 39(3), 413–425. Retrieved from <https://doi.org/10.5194/angeo-39-413-2021> doi: 10.5194/angeo-39-413-2021
- Katsavrias, C., Sandberg, I., Li, W., Podladchikova, O., Daglis, I., Papadimitriou, C., ... Aminalragia-Giamini, S. (2019, June). Highly relativistic electron flux enhancement during the weak geomagnetic storm of april–may 2017. *Journal of Geophysical Research: Space Physics*, 124(6), 4402–4413. Retrieved from <https://doi.org/10.1029/2019ja026743> doi: 10.1029/2019ja026743
- Li, W., Ma, Q., Thorne, R. M., Bortnik, J., Zhang, X.-J., Li, J., ... Goldstein, J. (2016, June). Radiation belt electron acceleration during the 17 march 2015 geomagnetic storm: Observations and simulations. *Journal of Geophysical Research: Space Physics*, 121(6), 5520–5536. Retrieved from <https://doi.org/10.1002/2016ja022400> doi: 10.1002/2016ja022400
- Li, X., Baker, D. N., Kanekal, S. G., Looper, M., & Temerin, M. (2001, October). Long term measurements of radiation belts by SAMPEX and their variations. *Geophysical Research Letters*, 28(20), 3827–3830. Retrieved from <https://doi.org/10.1029/2001gl013586> doi: 10.1029/2001gl013586
- Nasi, A., Daglis, I., Katsavrias, C., & Li, W. (2020, November). Interplay of source/seed electrons and wave-particle interactions in producing relativistic electron PSD enhancements in the outer van allen belt. *Journal of Atmospheric and Solar-Terrestrial Physics*, 210, 105405. Retrieved from <https://doi.org/10.1016/j.jastp.2020.105405> doi: 10.1016/j.jastp.2020.105405
- Newell, P. T., Sotirelis, T., Liou, K., Meng, C.-I., & Rich, F. J. (2007, January). A nearly universal solar wind-magnetosphere coupling function inferred from 10 magnetospheric state variables. *Journal of Geophysical Research: Space Physics*, 112(A1), n/a–n/a. Retrieved from <https://doi.org/10.1029/2006ja012015> doi: 10.1029/2006ja012015
- Onsager, T., Grubb, R., Kunches, J., Matheson, L., Speich, D., Zwickl, R. W., & Sauer, H. (1996, October). titleoperational uses of the GOES energetic particle detectors/title. In E. R. Washwell (Ed.), *GOES-8 and beyond*. SPIE. Retrieved from <https://doi.org/10.1117/12.254075> doi: 10.1117/12.254075
- Reeves, G. D., & Daglis, I. A. (2016, November). Geospace magnetic storms and the van allen radiation belts. In *Waves, particles, and storms in geospace*

- (pp. 51–79). Oxford University Press. Retrieved from <https://doi.org/10.1093/acprof:oso/9780198705246.003.0004> doi: 10.1093/acprof:oso/9780198705246.003.0004
- Rodgers, H. K., D.J., & Wrenn, G. (2003). The flumic electron environment model. In *Proceedings 8th sctc, huntsville*. 8th SCTC, Huntsville, USA.
- Russell, C. T., & McPherron, R. L. (1973, January). Semiannual variation of geomagnetic activity. *Journal of Geophysical Research*, 78(1), 92–108. Retrieved from <https://doi.org/10.1029/ja078i001p00092> doi: 10.1029/ja078i001p00092
- Sandberg, I., Daglis, I. A., Heynderickx, D., Truscott, P., Hands, A., Evans, H., & Nieminen, P. (2014, August). Development and validation of the electron slot region radiation environment model. *IEEE Transactions on Nuclear Science*, 61(4), 1656–1662. Retrieved from <https://doi.org/10.1109/tns.2014.2304982> doi: 10.1109/tns.2014.2304982
- Sandberg, I., Jiggins, P., Evans, H., Papadimitriou, C., Amini, S., Katsavrias, C., ... Daglis, I. A. (2021, June). Harmonization of RBSP and arase energetic electron measurements utilizing ESA radiation monitor data. *Space Weather*, 19(6). Retrieved from <https://doi.org/10.1029/2020sw002692> doi: 10.1029/2020sw002692
- Sicard, A., Boscher, D., Bourdarie, S., Lazaro, D., Standarovski, D., & Ecoffet, R. (2018, July). GREEN: the new global radiation earth ENvironment model (beta version). *Annales Geophysicae*, 36(4), 953–967. Retrieved from <https://doi.org/10.5194/angeo-36-953-2018> doi: 10.5194/angeo-36-953-2018
- Sicard-Piet, A., Bourdarie, S., Boscher, D., Friedel, R. H. W., Thomsen, M., Goka, T., ... Koshiishi, H. (2008, July). A new international geostationary electron model: IGE-2006, from 1 keV to 5.2 MeV. *Space Weather*, 6(7), n/a–n/a. Retrieved from <https://doi.org/10.1029/2007sw000368> doi: 10.1029/2007sw000368
- Smirnov, A. G., Berrendorf, M., Shprits, Y. Y., Kronberg, E. A., Allison, H. J., Aseev, N. A., ... Effenberger, F. (2020, October). Medium energy electron flux in earths outer radiation belt (MERLIN): A machine learning model. *Space Weather*, 18(11). Retrieved from <https://doi.org/10.1029/2020sw002532> doi: 10.1029/2020sw002532
- Subbotin, D. A., & Shprits, Y. Y. (2009, October). Three-dimensional modeling of the radiation belts using the versatile electron radiation belt (VERB) code. *Space Weather*, 7(10), n/a–n/a. Retrieved from <https://doi.org/10.1029/2008sw000452> doi: 10.1029/2008sw000452
- Thomsen, M. F., Henderson, M. G., & Jordanova, V. K. (2013, May). Statistical properties of the surface-charging environment at geosynchronous orbit. *Space Weather*, 11(5), 237–244. Retrieved from <https://doi.org/10.1002/swe.20049> doi: 10.1002/swe.20049
- Tsyganenko, N. A. (2005). Modeling the dynamics of the inner magnetosphere during strong geomagnetic storms. *Journal of Geophysical Research*, 110(A3). Retrieved from <https://doi.org/10.1029/2004ja010798> doi: 10.1029/2004ja010798
- Varotsou, A., Boscher, D., Bourdarie, S., Horne, R. B., Glauert, S. A., & Meredith, N. P. (2005, October). Simulation of the outer radiation belt electrons near geosynchronous orbit including both radial diffusion and resonant interaction with whistler-mode chorus waves. *Geophysical Research Letters*, 32(19), n/a–n/a. Retrieved from <https://doi.org/10.1029/2005gl023282> doi: 10.1029/2005gl023282
- Varotsou, A., Boscher, D., Bourdarie, S., Horne, R. B., Meredith, N. P., Glauert, S. A., & Friedel, R. H. (2008, December). Three-dimensional test simulations of the outer radiation belt electron dynamics including electron-chorus resonant interactions. *Journal of Geophysical Research: Space Physics*, 113(A12),

615 n/a–n/a. Retrieved from <https://doi.org/10.1029/2007ja012862> doi:  
 616 10.1029/2007ja012862  
 617 Vette, J. I. (1991, November). *The AE-8 trapped electron model environment*. NASA  
 618 STI/Recon Technical Report N.  
 619 Zheng, Y., Ganushkina, N. Y., Jiggins, P., Jun, I., Meier, M., Minow, J. I., . . .  
 620 Kuznetsova, M. M. (2019, October). Space radiation and plasma ef-  
 621 fects on satellites and aviation: Quantities and metrics for tracking per-  
 622 formance of space weather environment models. *Space Weather*, 17(10),  
 623 1384–1403. Retrieved from <https://doi.org/10.1029/2018sw002042> doi:  
 624 10.1029/2018sw002042

Figure 1.



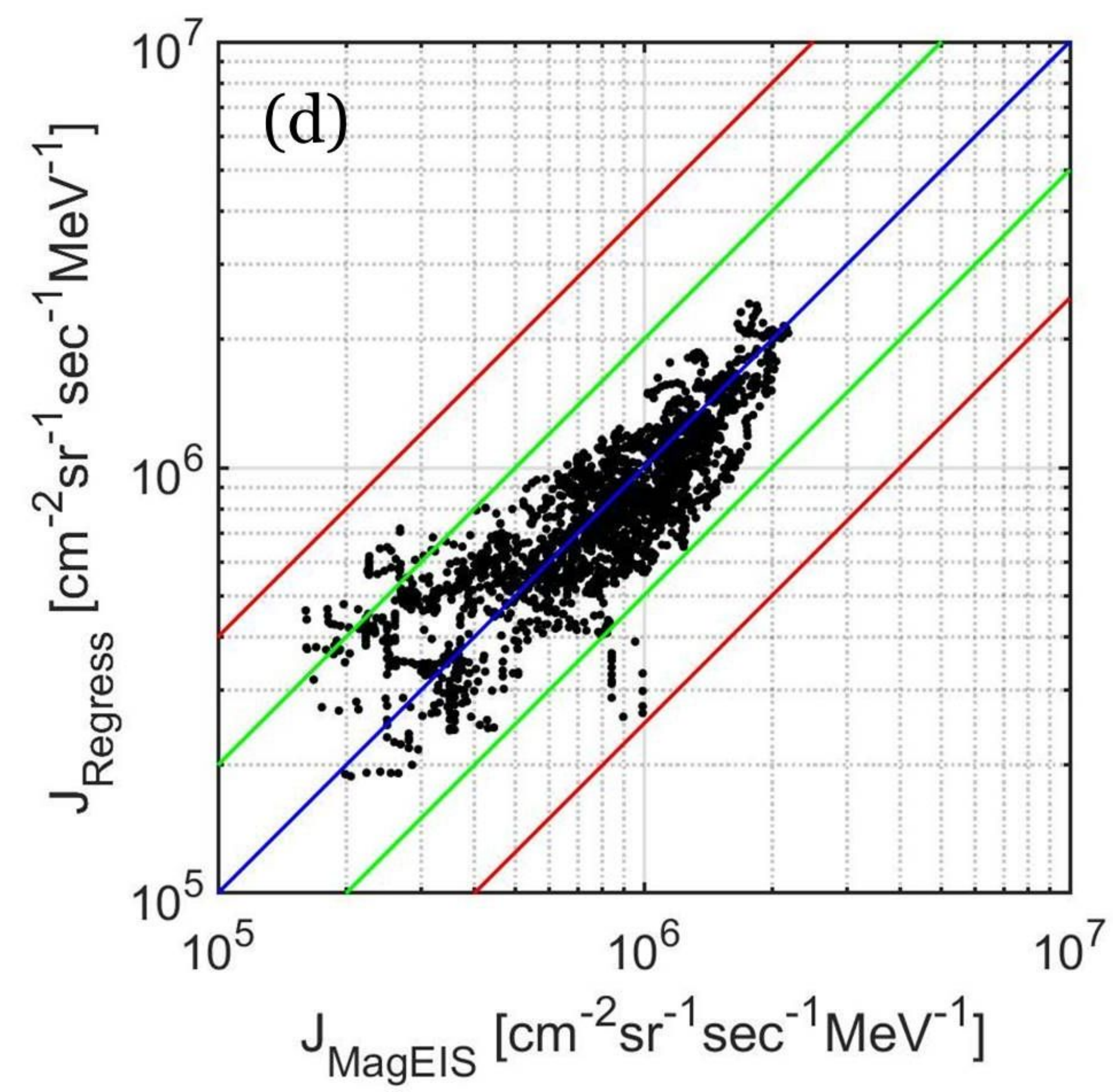
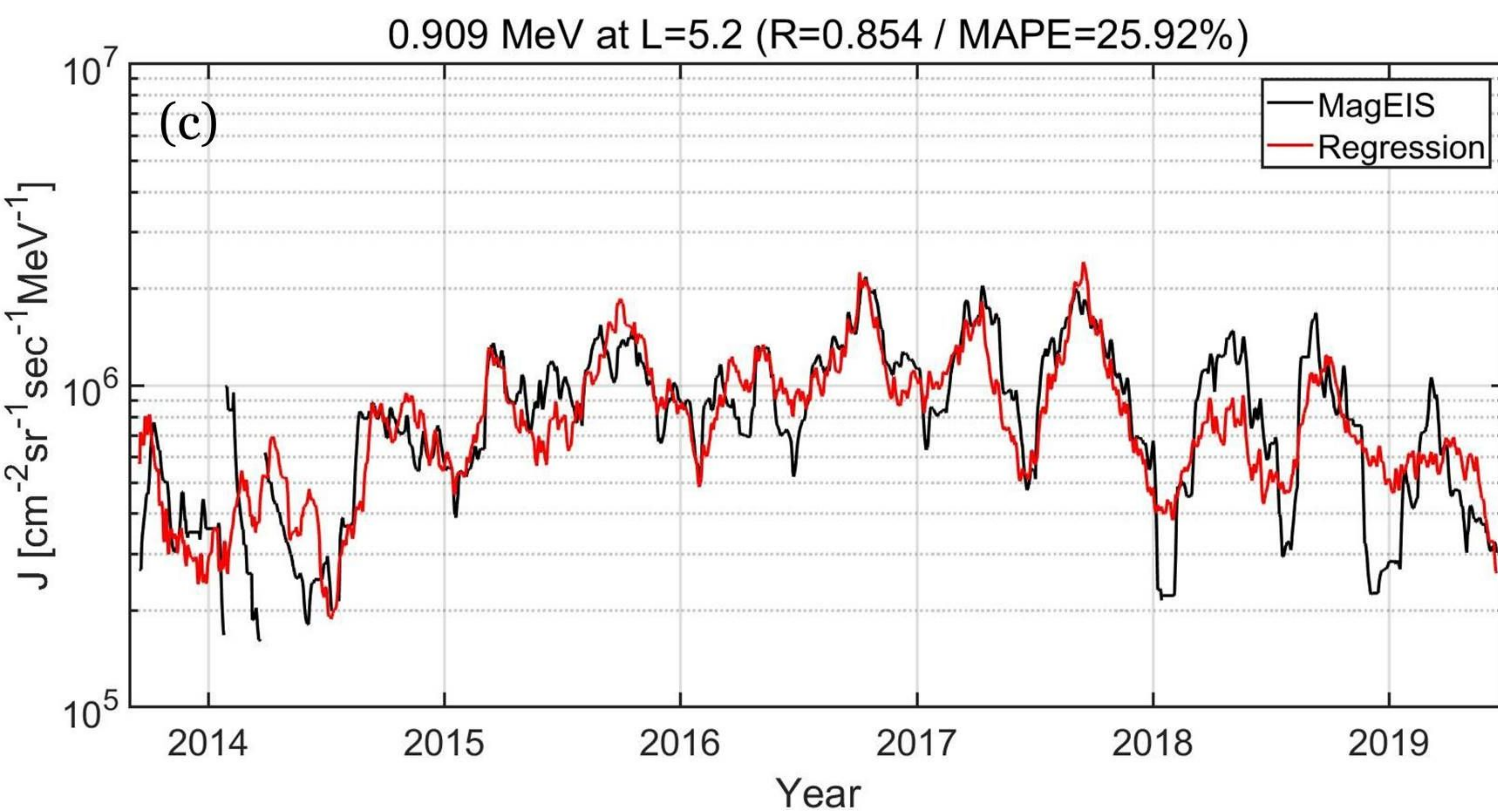
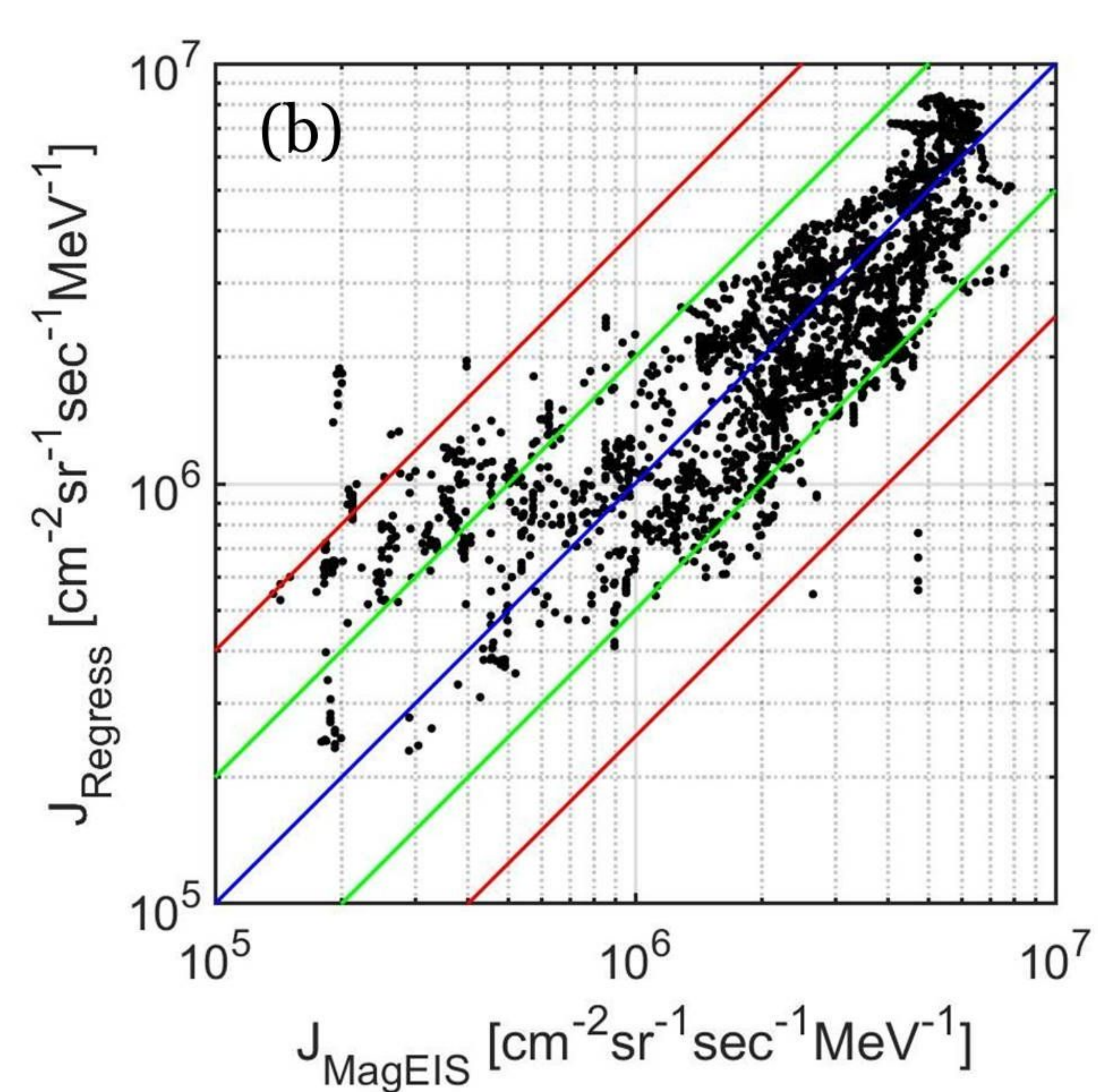
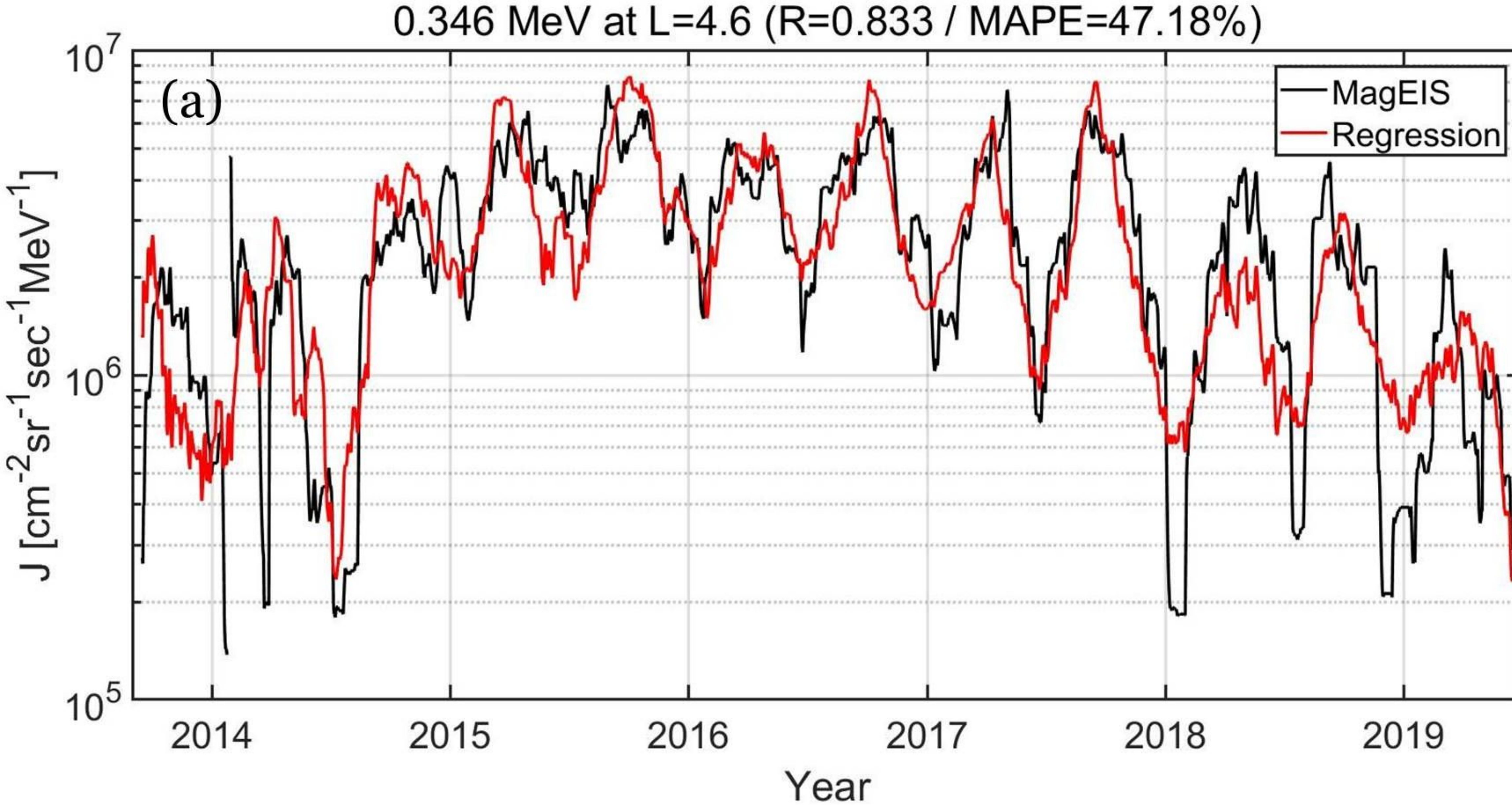




Figure 2.



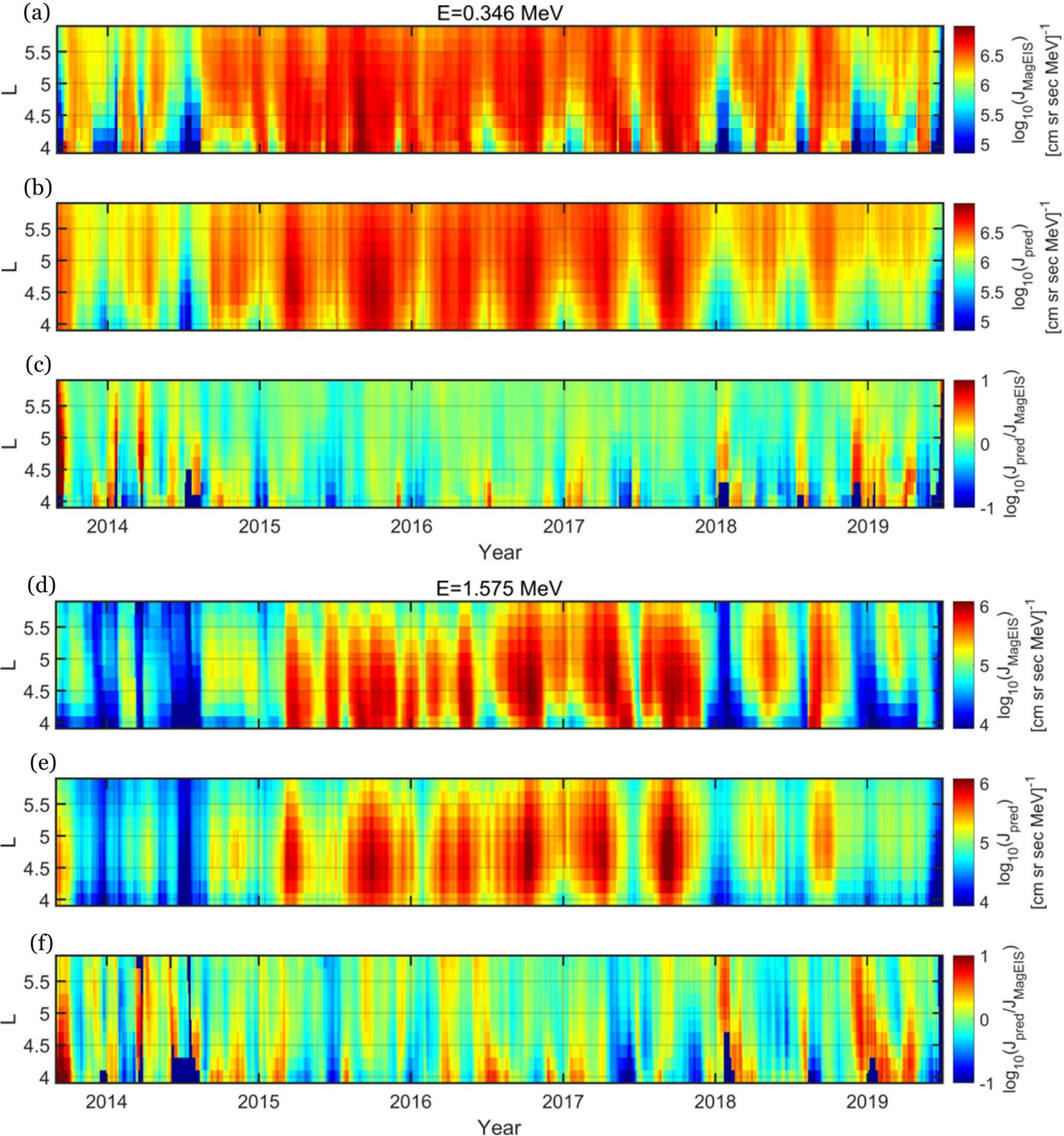




Figure 3.



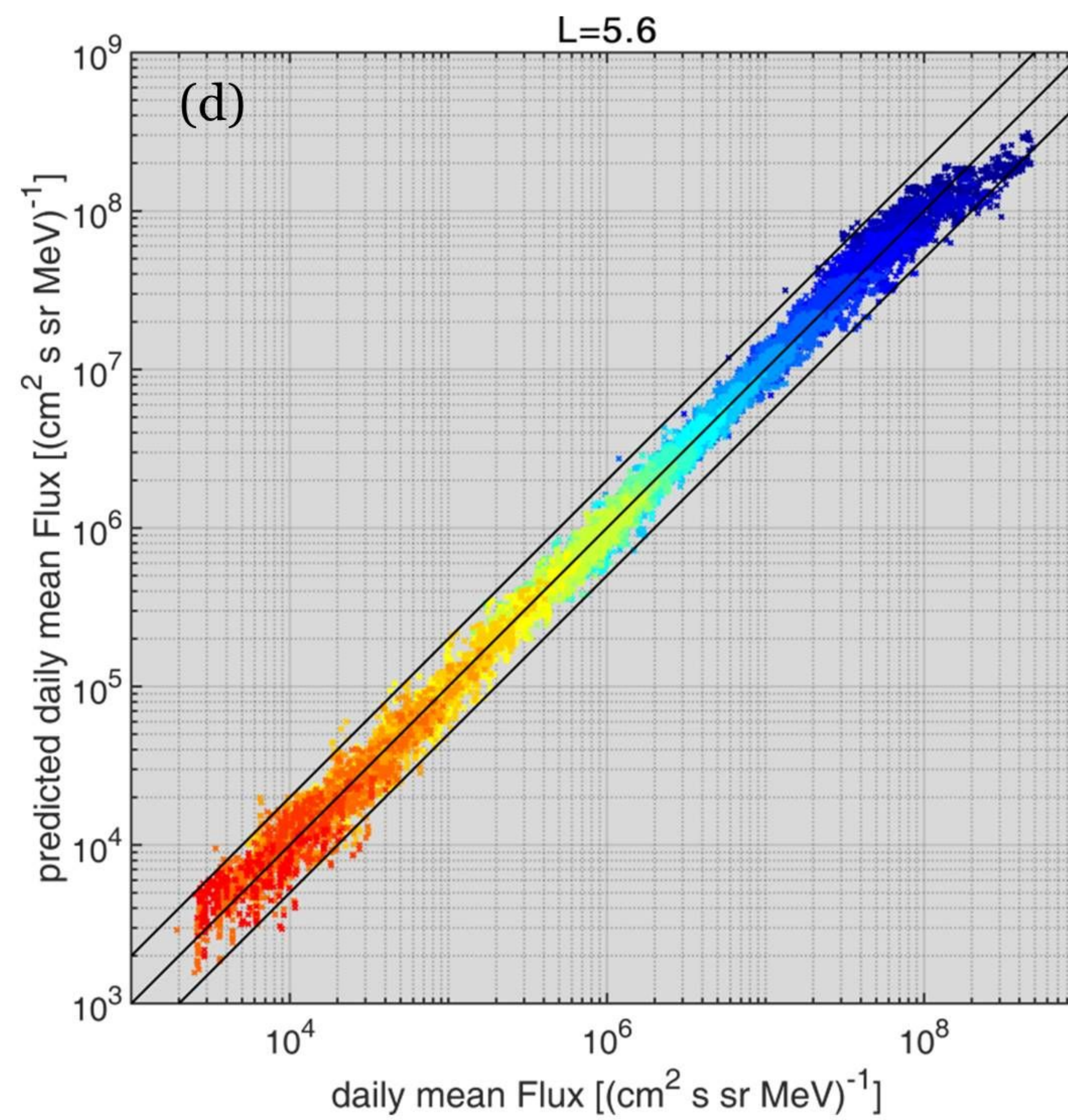
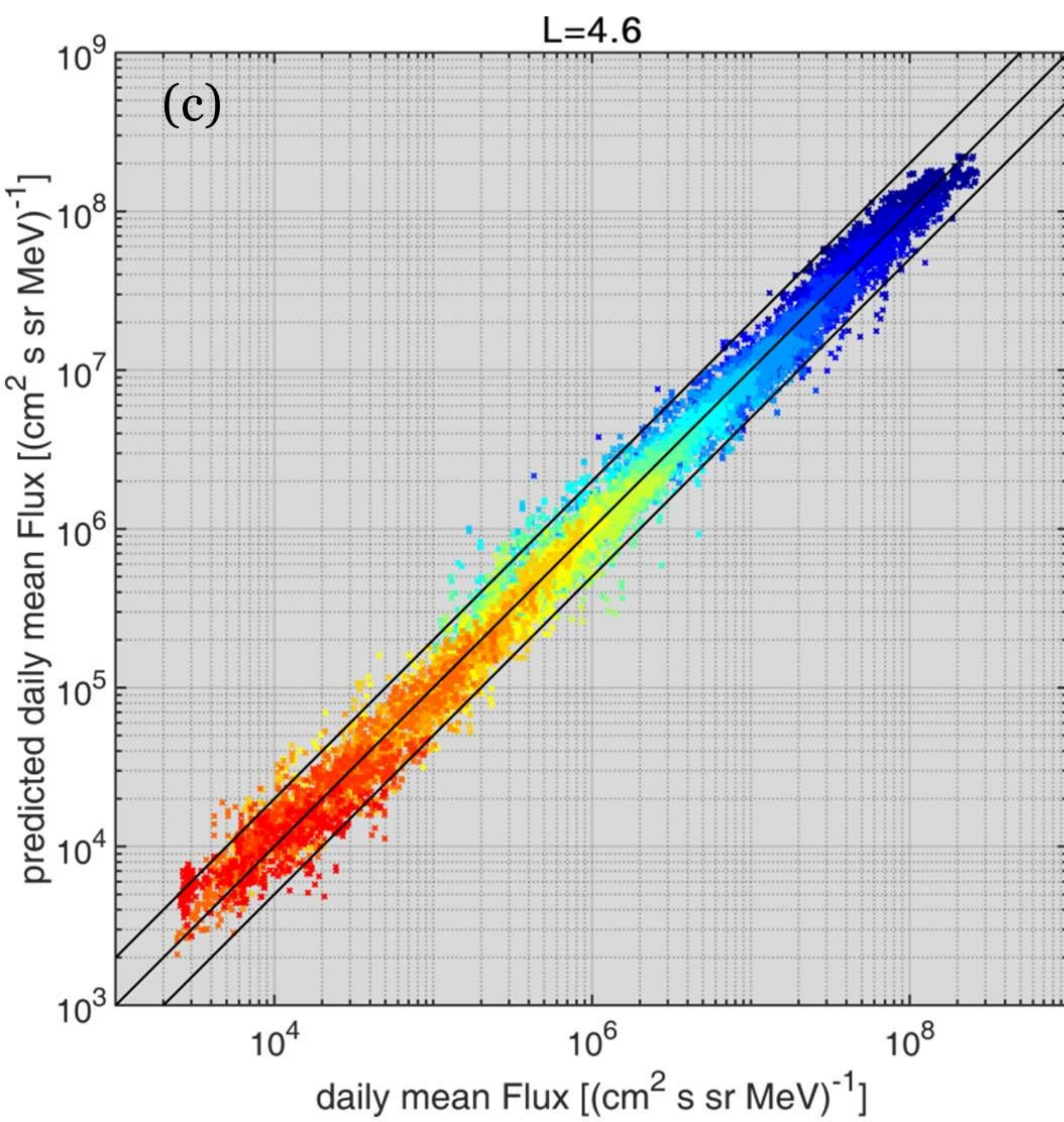
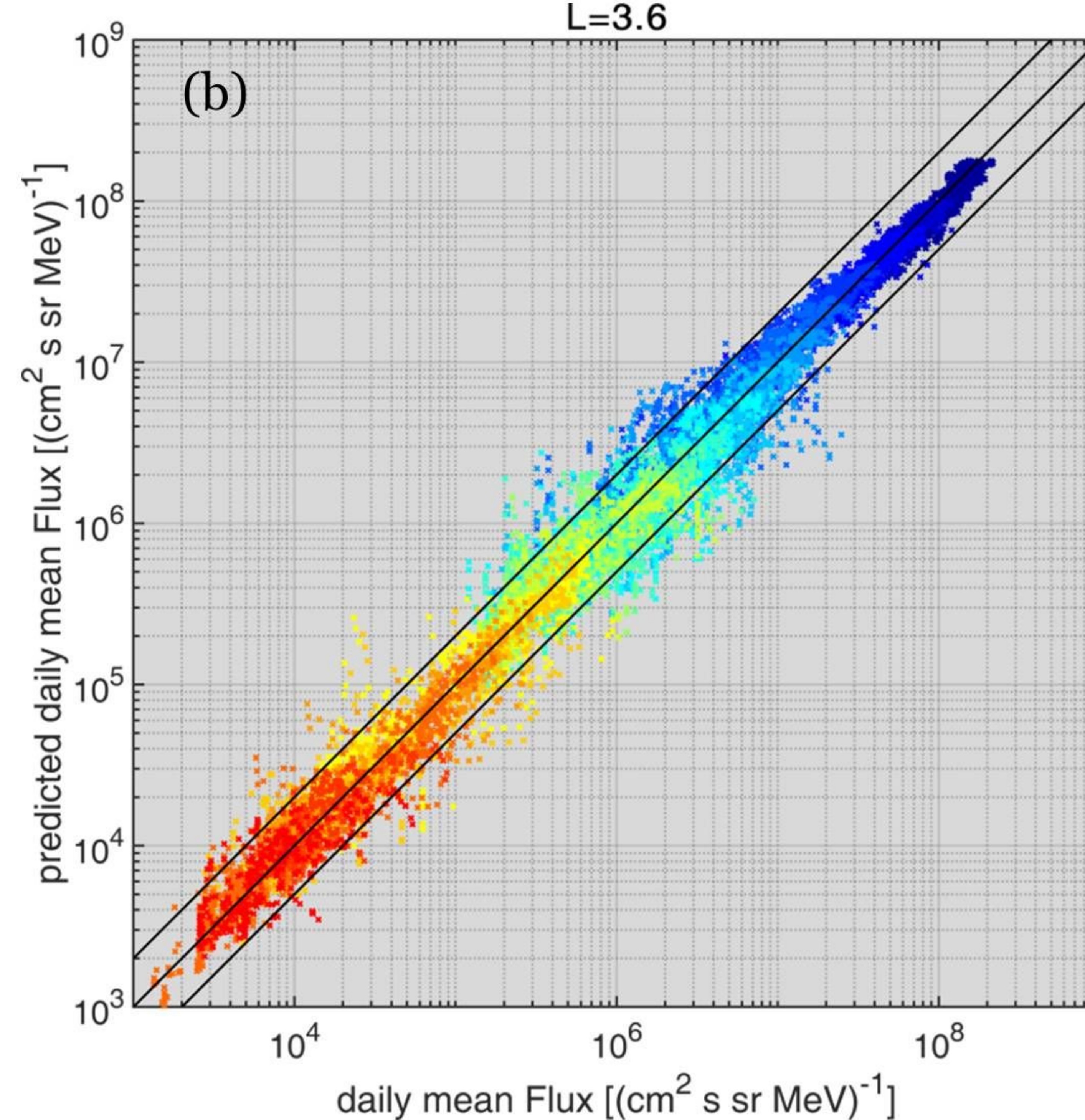
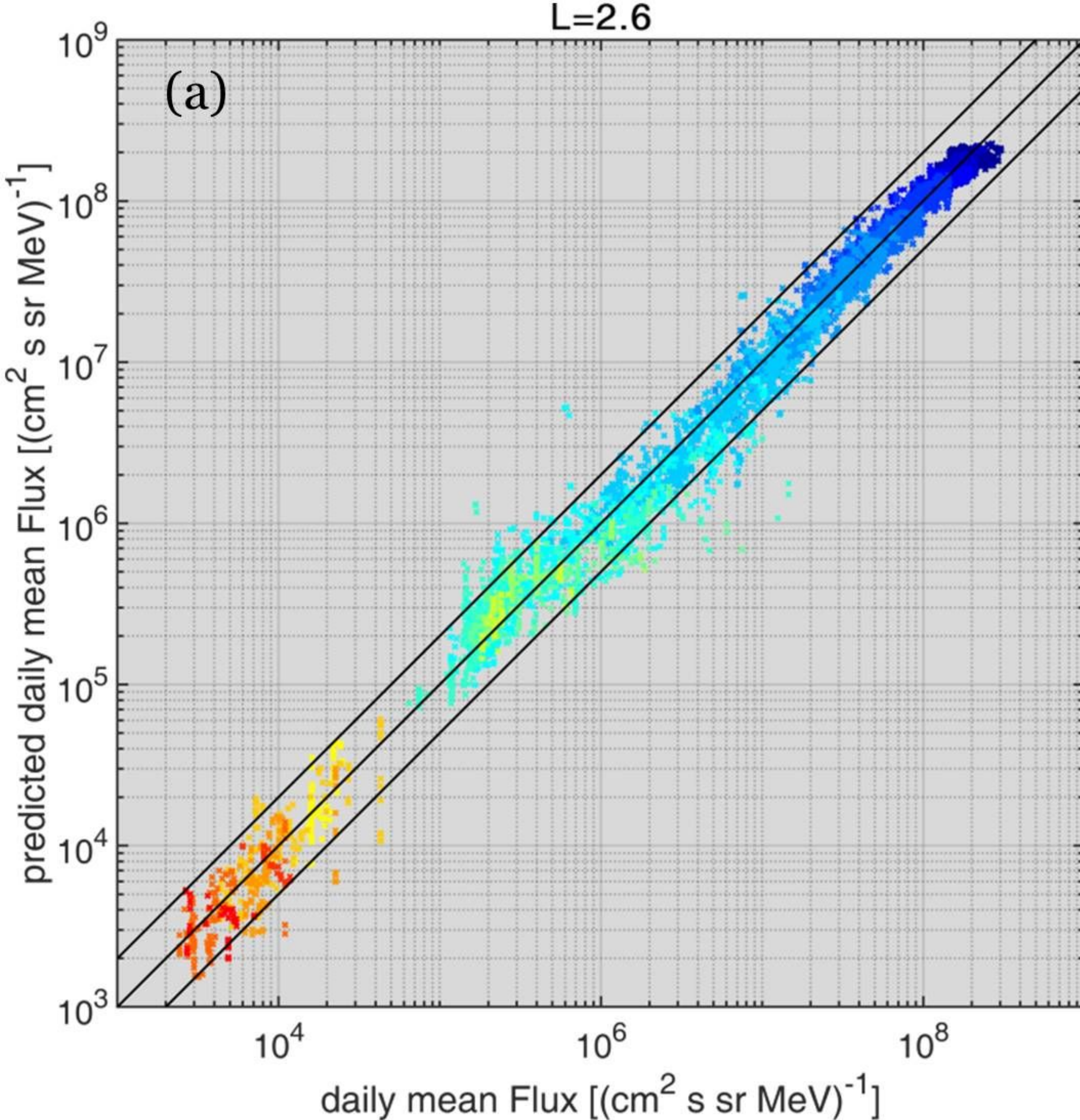




Figure 4.



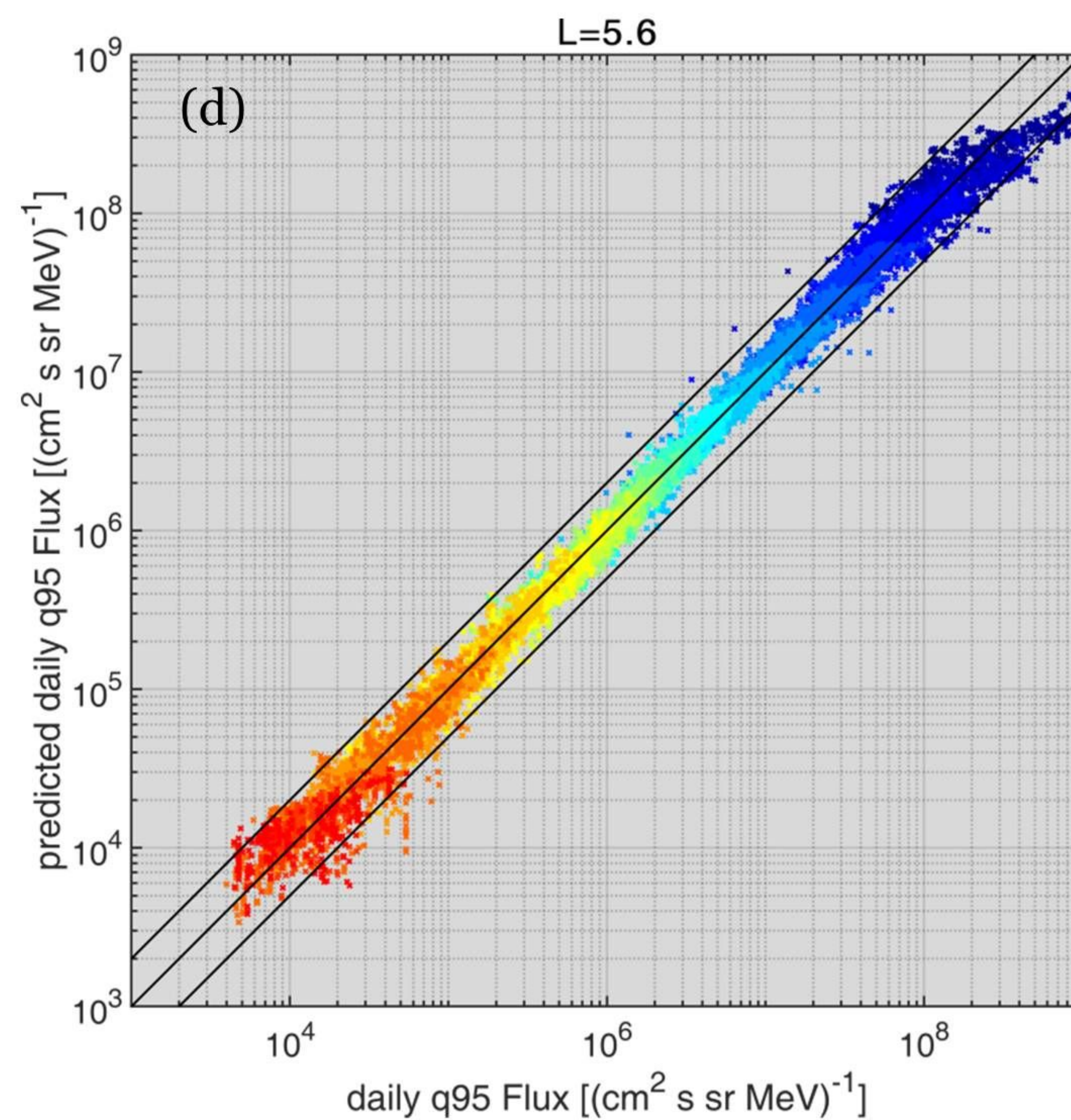
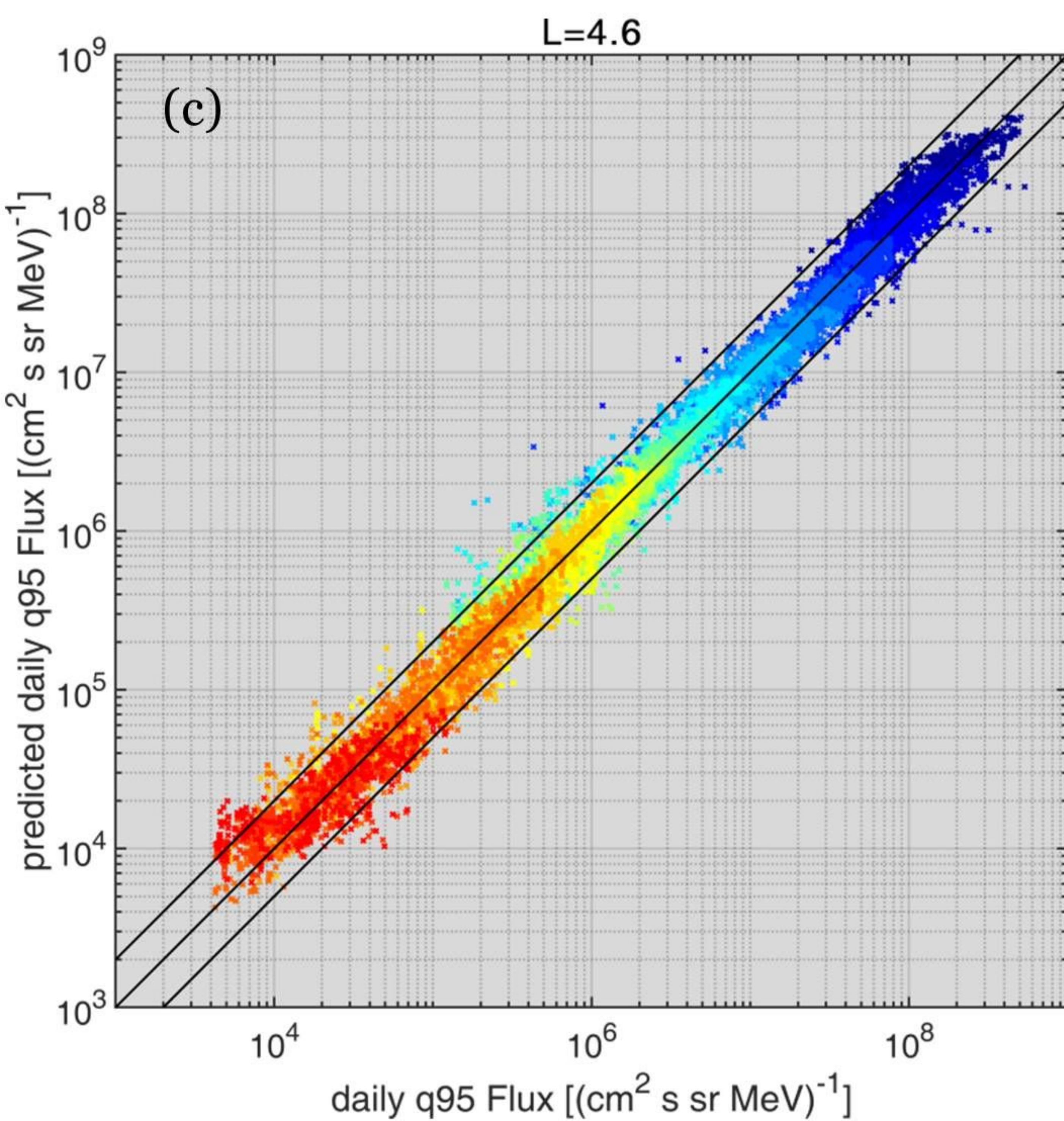
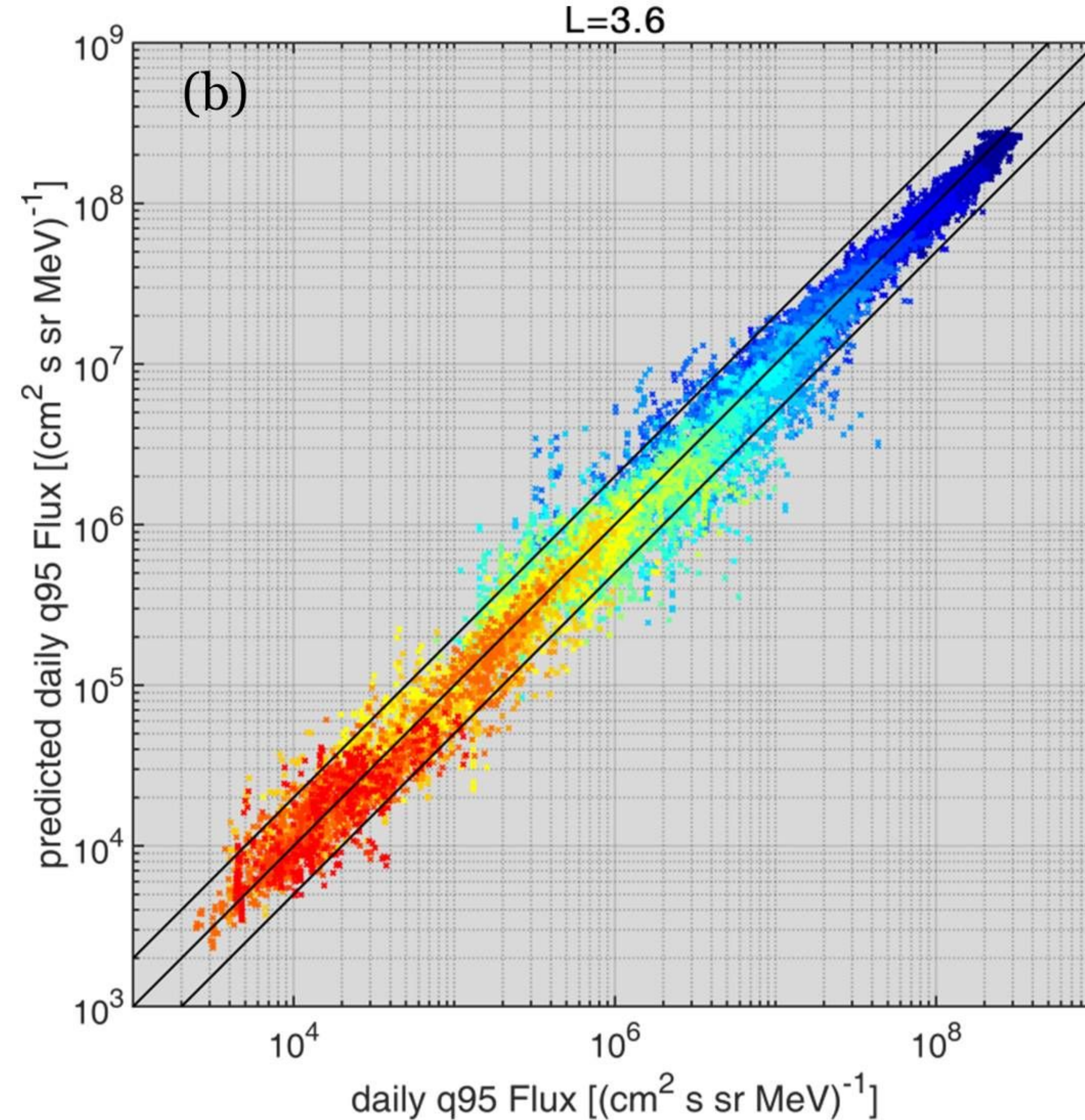
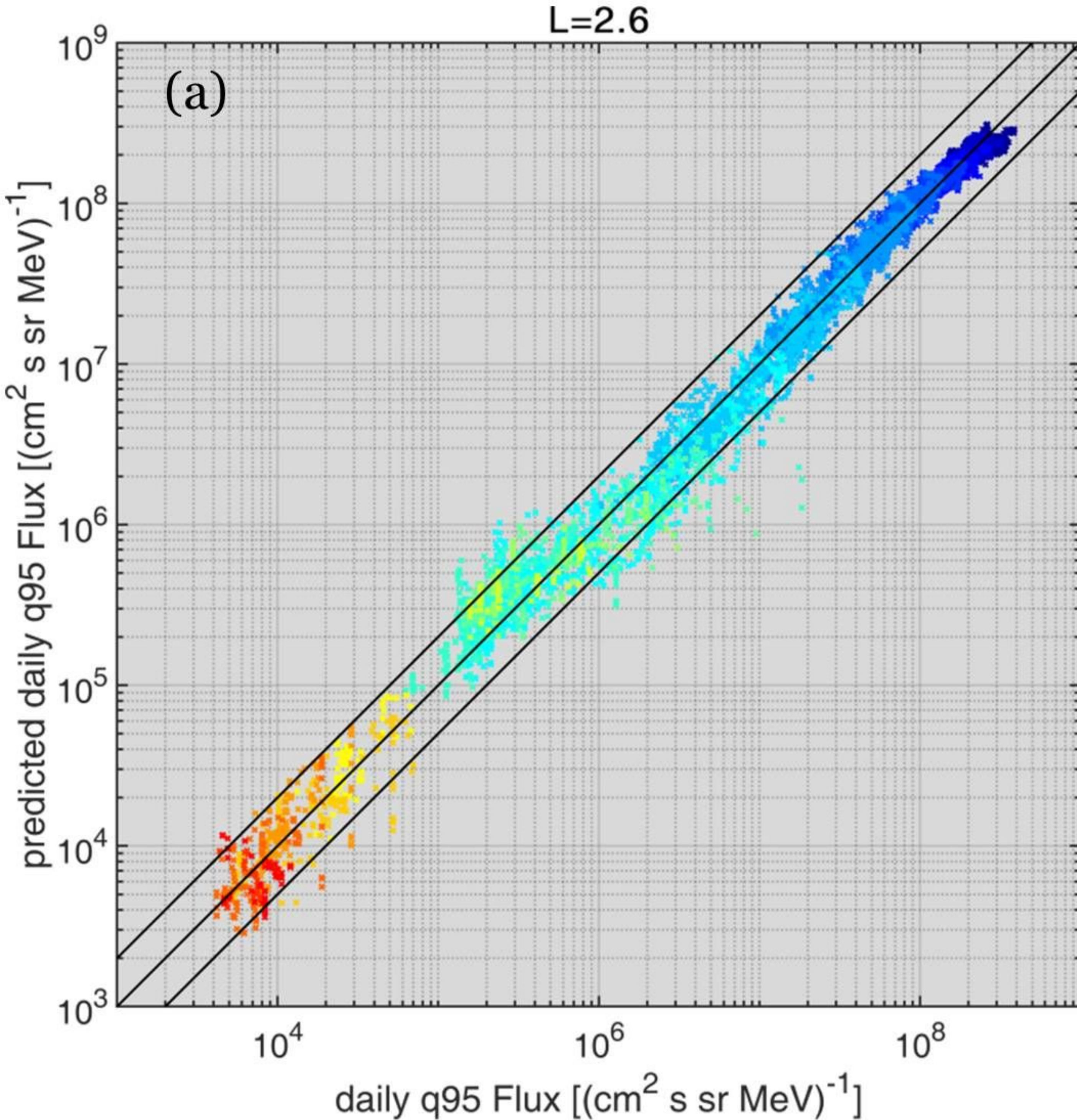




Figure 5.



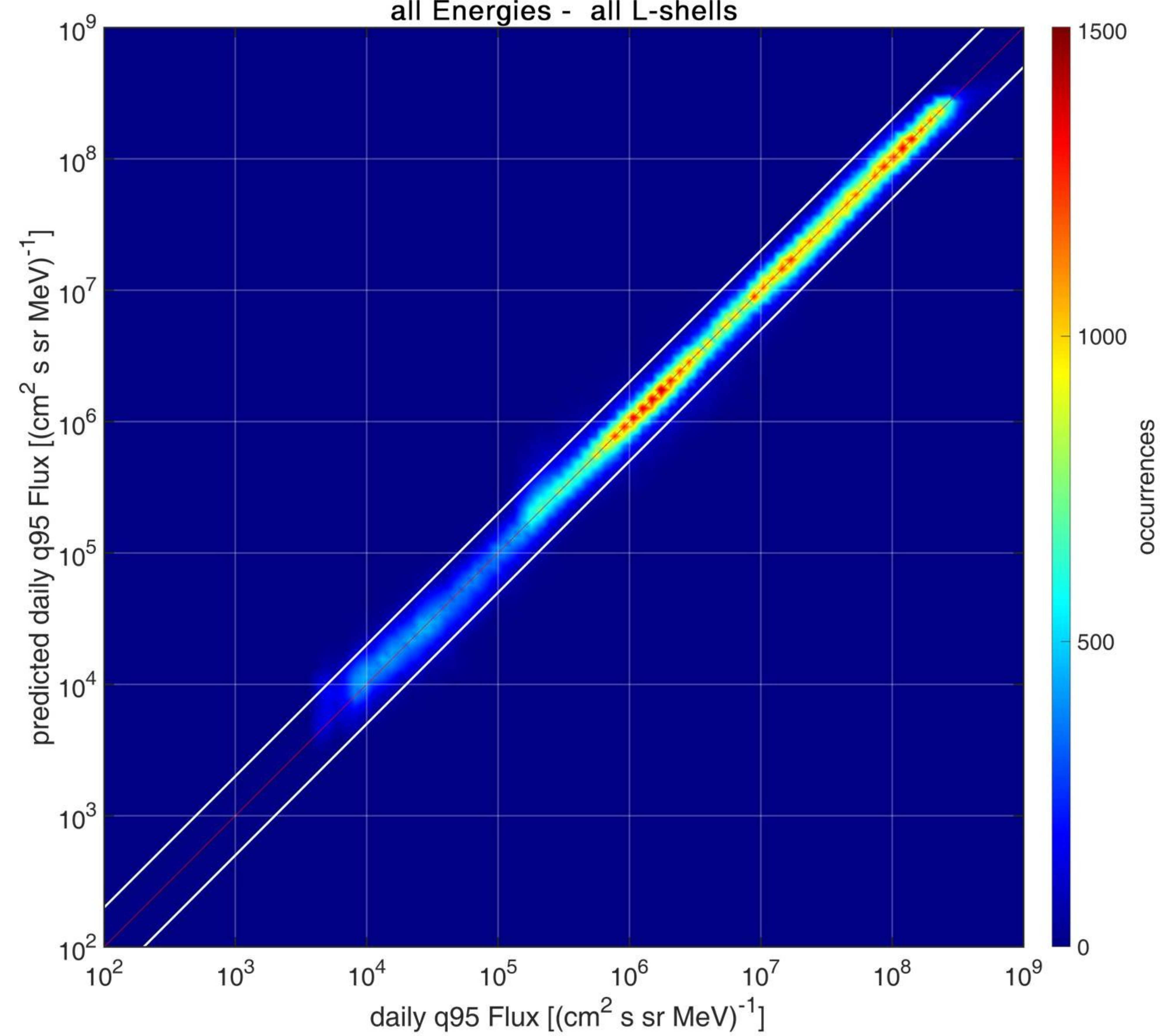
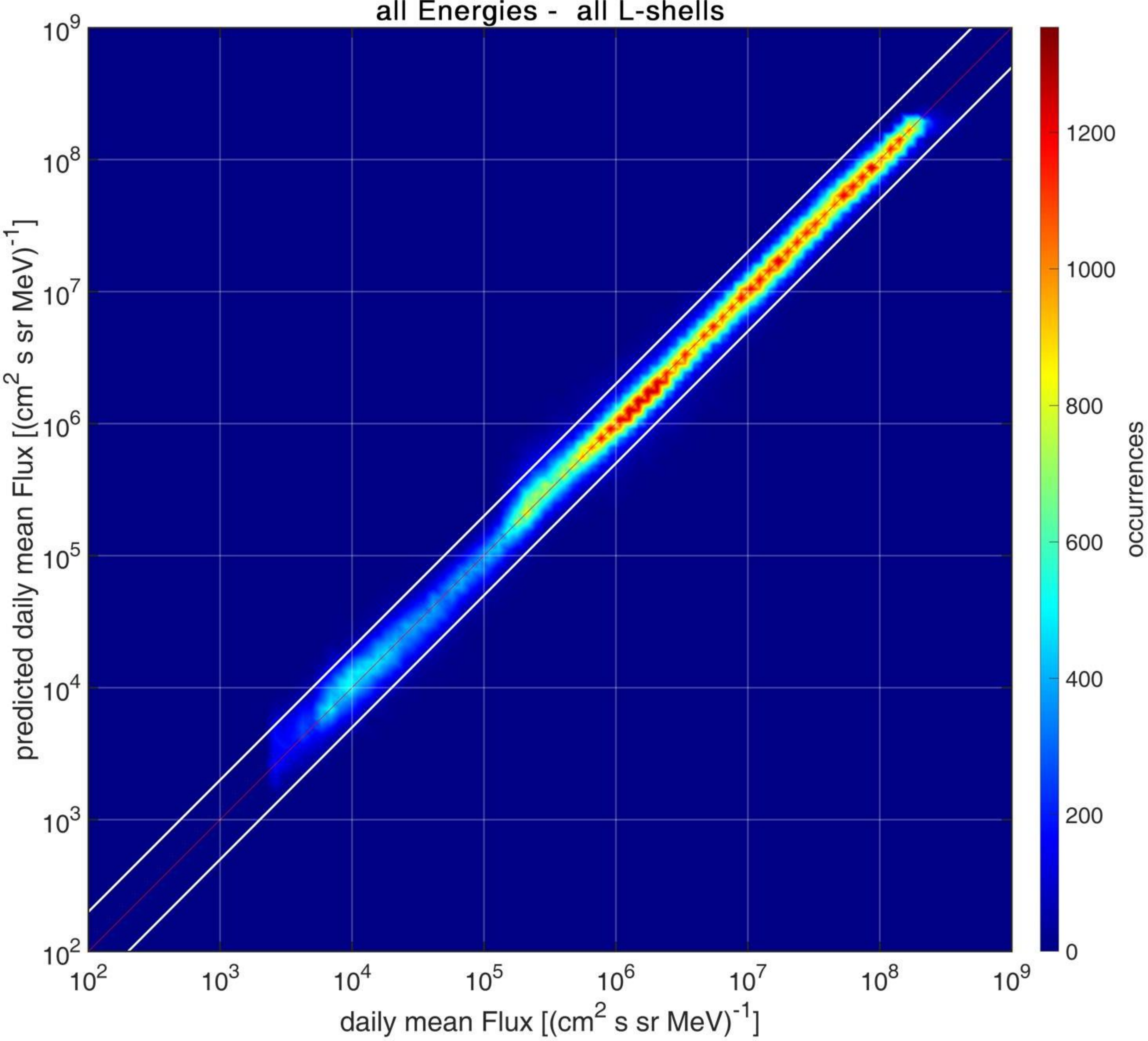
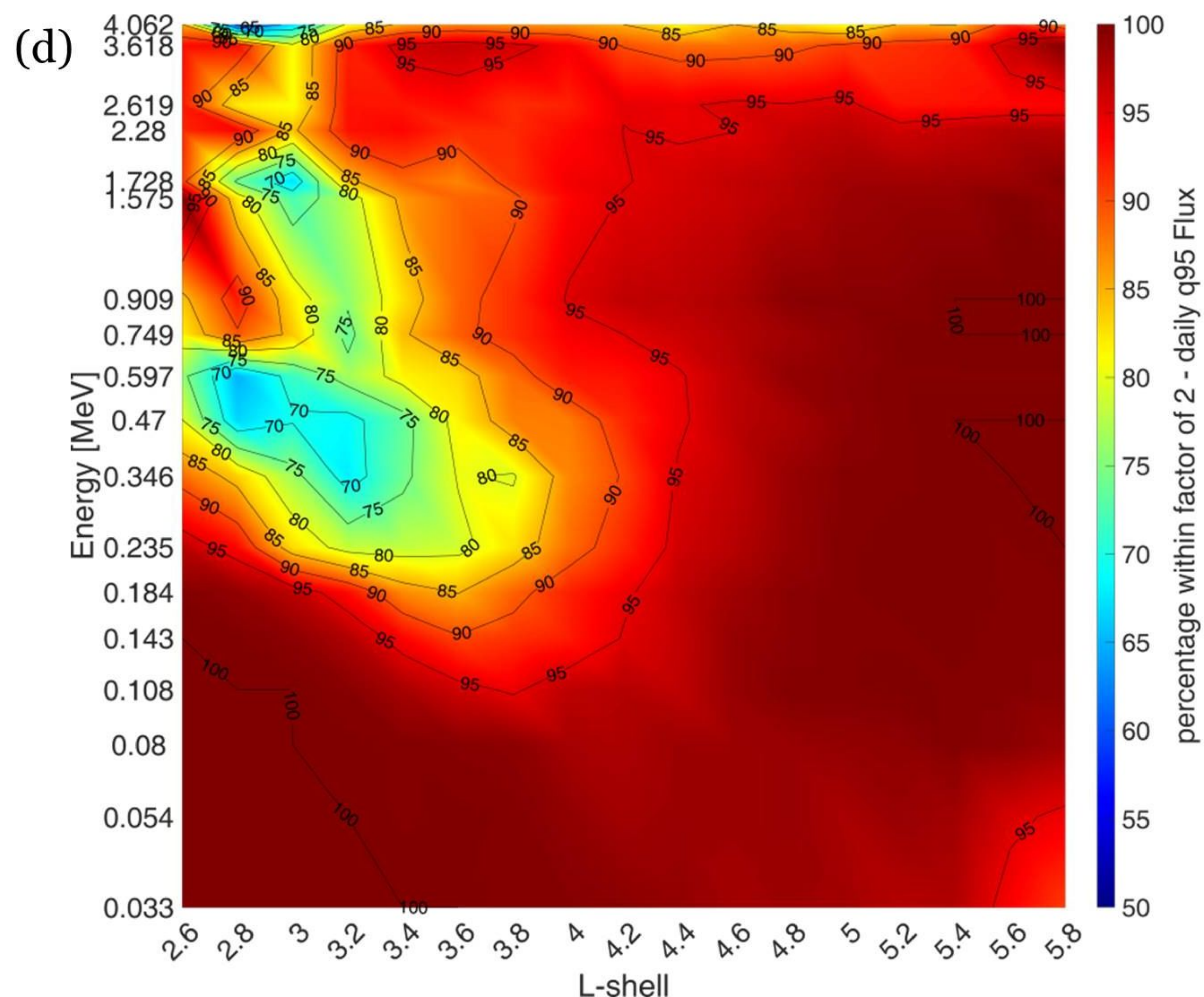
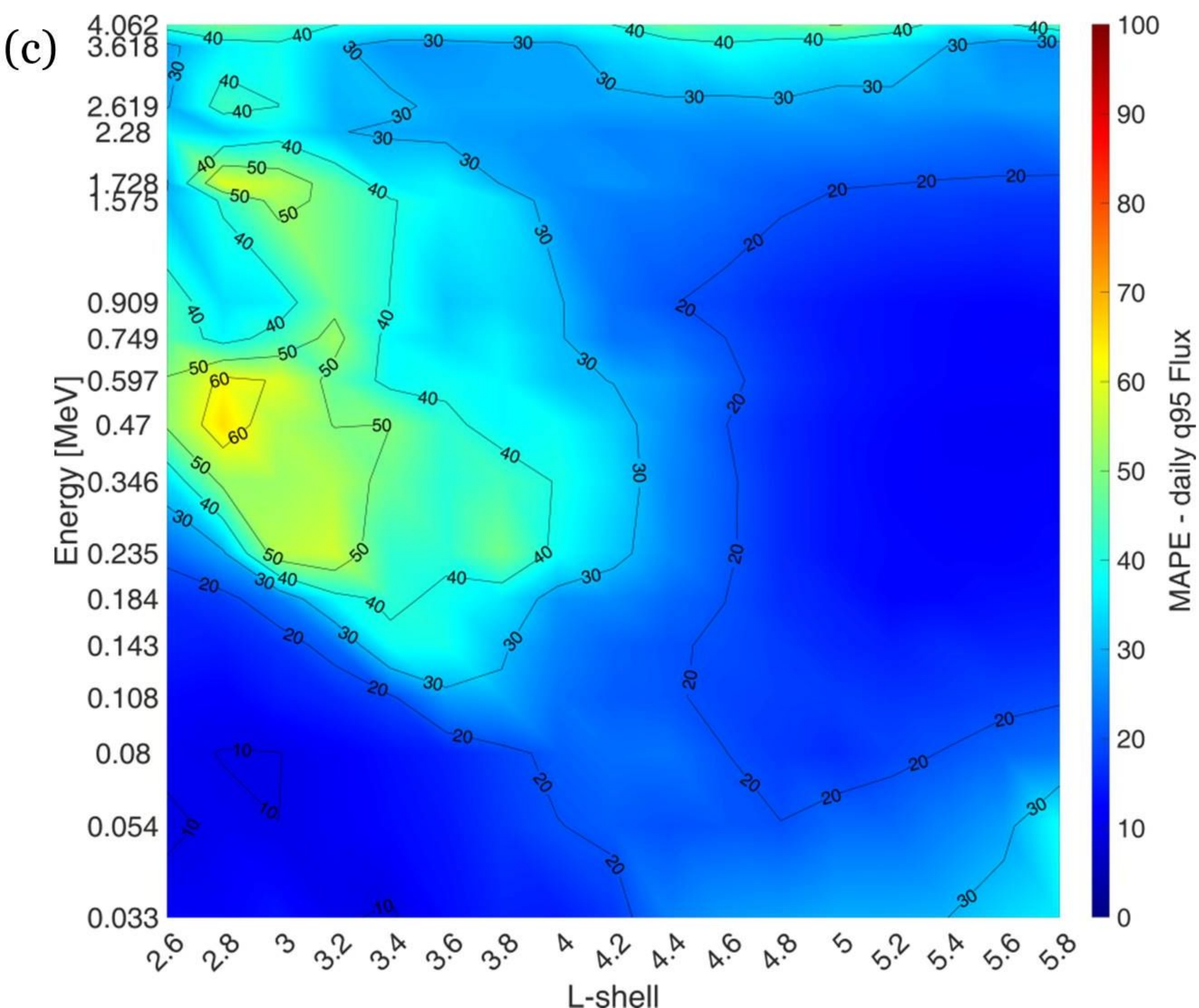
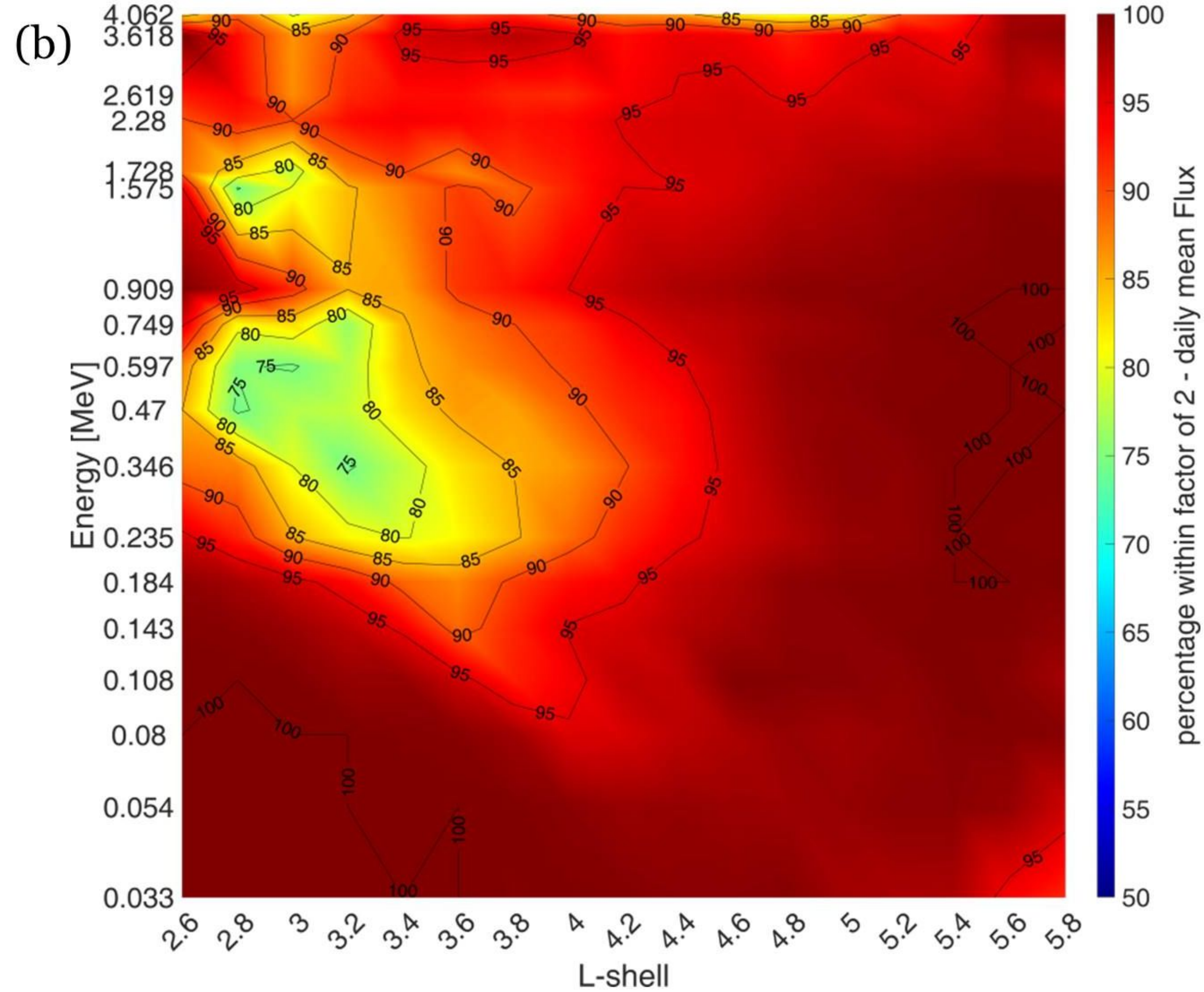
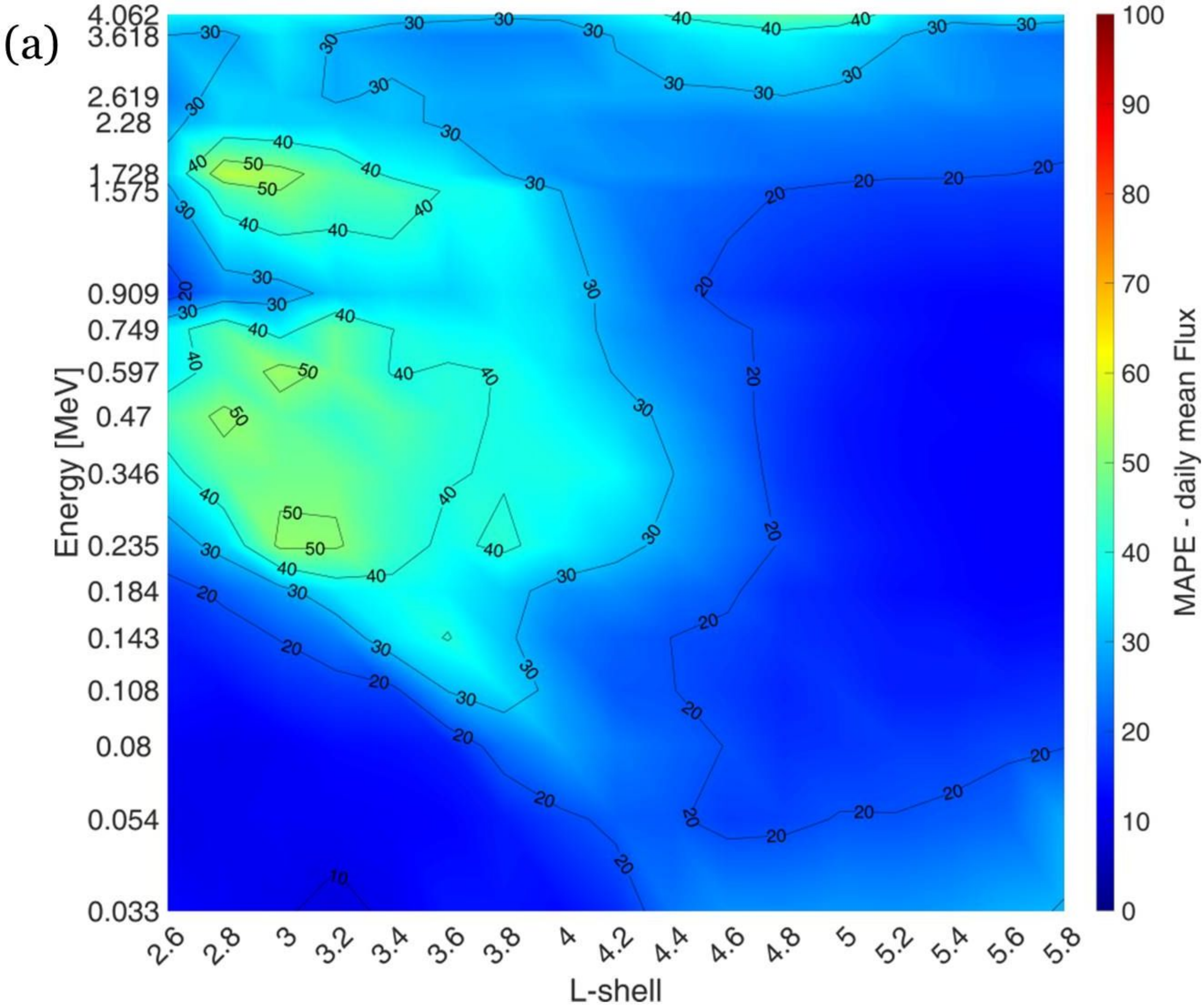




Figure 6.







**Figure 7.**



